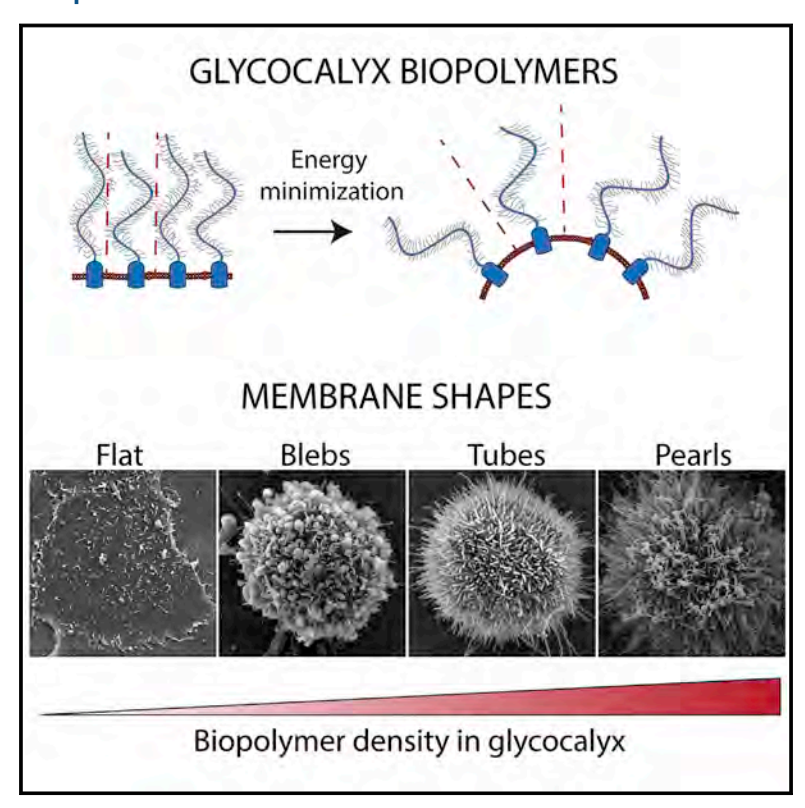


Physical Principles of Membrane Shape Regulation by the Glycocalyx

Graphical Abstract



Authors

Carolyn R. Shurer, Joe Chin-Hun Kuo, LaDeidra Monét Roberts, ..., Gerald W. Feigenson, Heidi L. Reesink, Matthew J. Paszek

Correspondence

mjp31@cornell.edu

In Brief

The extracellular glycocalyx can impose forces that bend the plasma membrane and regulate projections and vesicle formation.

Highlights

- Biopolymers in the glycocalyx can generate forces that bend the plasma membrane
- Glycocalyx polymers regulate formation of membrane projections and microvesicles
- Both intracellular dynamics and glycocalyx-imposed forces regulate membrane shapes
- Polymer theories explain effects of polymer size/density on membrane morphologies





Physical Principles of Membrane Shape Regulation by the Glycocalyx

Carolyn R. Shurer,^{1,11} Joe Chin-Hun Kuo,^{1,11} LaDeidra Monét Roberts,^{2,11} Jay G. Gandhi,¹ Marshall J. Colville,³ Thais A. Enoki,⁴ Hao Pan,³ Jin Su,⁵ Jade M. Noble,¹ Michael J. Hollander,¹ John P. O'Donnell,⁶ Rose Yin,¹ Kayvon Pedram,⁷ Leonhard Möckl,⁷ Lena F. Kourkoutis,^{8,9} W.E. Moerner,⁷ Carolyn R. Bertozzi,^{7,10} Gerald W. Feigenson,^{3,4} Heidi L. Reesink,⁵ and Matthew J. Paszek^{1,2,3,9,12,*}

¹Robert Frederick Smith School of Chemical and Biomolecular Engineering, Cornell University, Ithaca, NY 14853, USA

SUMMARY

Cells bend their plasma membranes into highly curved forms to interact with the local environment, but how shape generation is regulated is not fully resolved. Here, we report a synergy between shape-generating processes in the cell interior and the external organization and composition of the cell-surface glycocalyx. Mucin biopolymers and long-chain polysaccharides within the glycocalyx can generate entropic forces that favor or disfavor the projection of spherical and finger-like extensions from the cell surface. A polymer brush model of the glycocalyx successfully predicts the effects of polymer size and cell-surface density on membrane morphologies. Specific glycocalyx compositions can also induce plasma membrane instabilities to generate more exotic undulating and pearled membrane structures and drive secretion of extracellular vesicles. Together, our results suggest a fundamental role for the glycocalyx in regulating curved membrane features that serve in communication between cells and with the extracellular matrix.

INTRODUCTION

Tubular and spherical extensions of the plasma membrane play vital roles in human development and everyday cellular functions. Although curved membrane protrusions have long been recognized to increase cell-surface area for secretion, absorption, and receptor-mediated communication, modern research has provided compelling examples of more diverse and sophis-

ticated functionalities (Marshall, 2012). For instance, membrane projections are generated by embryonic cells to pinpoint delivery of morphogens at distant sites in developing tissues (Bischoff et al., 2013; Kornberg and Roy, 2014) and also by native and engineered immune cells for antigen surveillance (D'Aloia et al., 2018; Jung et al., 2016). Deregulation of membrane-shape-generating processes can contribute directly to disease progression. Notably, aggressive tumor cells extend abundant membrane tubules for adhesion and long-range intercellular communication, project spherical blebs to generate friction for amoeboid migration, and generate spherical microvesicles at the plasma membrane for long-range delivery of cargoes (Antonyak et al., 2011; Becker et al., 2016; Bergert et al., 2015; Friedl and Wolf, 2010; Kramer and Nicolson, 1979; Liu et al., 2018; Lou et al., 2012).

Forces originating from cytoskeletal dynamics are posited to generate membrane curvature for the diverse spherical and tubular structures on the cell surface. Polymerizing cytoskeletal filaments are envisioned to push out at discrete points along the plasma membrane for extension of microvilli, cilia, filopodia, and other finger-like projections (Footer et al., 2007; Gupton and Gertler, 2007; Mogilner and Rubinstein, 2005; Peskin et al., 1993). Contraction of the cytoskeleton generates the hydrostatic pressure for spherical expansion of the membrane during bleb formation (Charras et al., 2005). The physical dynamics that bend sub-regions of the plasma membrane into microvesicles remain poorly understood; however, reports have implicated the actin cytoskeleton in their biogenesis (Tricarico et al., 2017).

Although the cell-surface glycocalyx is not featured in canonical models of membrane-shape regulation, correlations abound between glycocalyx composition and cell-surface morphology in both normal and disease states. Polypeptide and sugar co-polymers called mucins are frequently anchored at high densities on the surfaces of epithelial microvilli (Hattrup and Gendler, 2008;



²Meinig School of Biomedical Engineering, Cornell University, Ithaca, NY 14853, USA

³Field of Biophysics, Cornell University, Ithaca, NY 14853, USA

⁴Department of Molecular Biology and Genetics, Cornell University, Ithaca, NY 14853, USA

⁵Department of Clinical Sciences, Cornell University, Ithaca, NY 14853, USA

⁶Department of Molecular Medicine, Cornell University, Ithaca, NY 14853, USA

Department of Chemistry, Stanford University, Stanford, CA 94305, USA

⁸School of Applied and Engineering Physics, Cornell University, Ithaca, NY 14853, USA

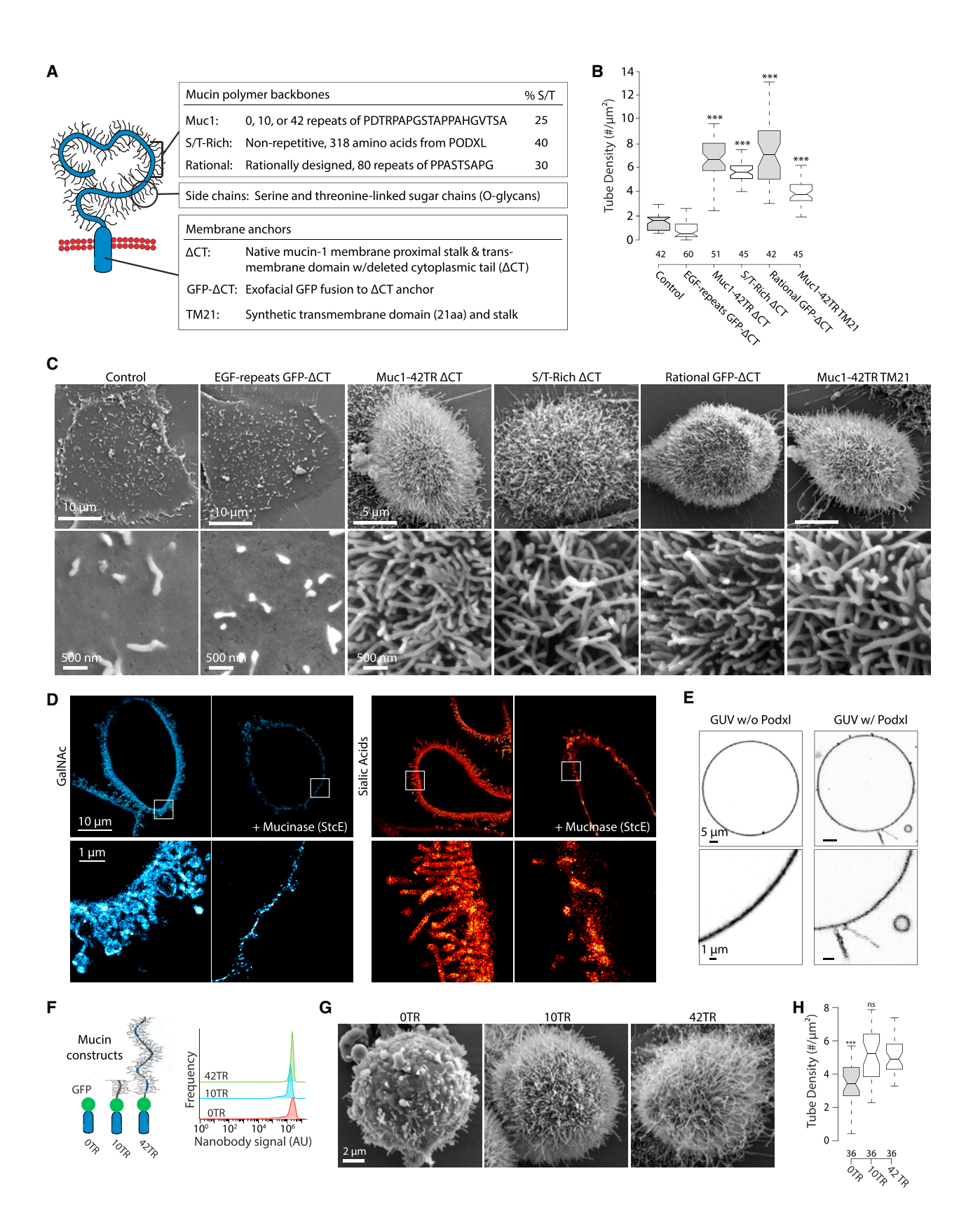
⁹Kavli Institute at Cornell for Nanoscale Science, Ithaca, NY 14853, USA

¹⁰Howard Hughes Medical Institute, Stanford University, Stanford, CA 94305, USA

¹¹These authors contributed equally

¹²Lead Contact

^{*}Correspondence: mjp31@cornell.edu https://doi.org/10.1016/j.cell.2019.04.017



(legend on next page)

Kesavan et al., 2009; Kesimer et al., 2013), cilia (Button et al., 2012), and filopodia (Bennett et al., 2001). Hyaluronan polymers densely coat the microvilli of oocytes and mesothelium (Evanko et al., 2007; Makabe et al., 2006). Chains of sialic acid and hyaluronan decorate the highly curved surfaces of neuronal axons (Fowke et al., 2017; van den Pol and Kim, 1993; Zhang et al., 1992). T cells and dendritic cells exhibit coincident changes in membrane tubularization and mucin expression upon maturation (Agrawal et al., 1998; Cloosen et al., 2004; Jung et al., 2016; Pilon et al., 2009). Tumor cells frequently produce an abundance of mucins and hyaluronan on their cell surface (Kufe, 2009; Turley et al., 2016), and the expression of these polymers has been linked to their unique membrane features, such as extensive microvilli (Koistinen et al., 2015; Polefka et al., 1984). Mucins and hyaluronan polymers are also densely arrayed on the surfaces of enterocytes, reactive astrocytes, dendritic cells, and tumor cells, and these cells commonly secrete high levels of vesicles (Cloosen et al., 2004; Gangoda et al., 2015; McConnell et al., 2009; Paszek et al., 2014; Pelaseyed et al., 2014; Tricarico et al., 2017). Although the ubiquity of these correlations suggests a possible causal relationship between glycocalyx polymer composition and plasma membrane morphologies, a specific mechanism of action has not been delineated.

Mucins and long-chain polysaccharides are anchored to the membrane, such that long polymer chains or loops are expected to extend from the cell surface (Hattrup and Gendler, 2008; Lee et al., 1993). The ensemble resembles a well-studied structure in polymer physics called a brush, where polymers are grafted on one end to a surface (Chen et al., 2017). Polymer brush theory has long recognized that steric interactions in a densely crowded brush restrict the number of molecular configurations each polymer can explore, thereby increasing the free energy of the system through reduced entropy (de Gennes, 1980). Similar to the thermodynamic basis of gas pressure, the entropic penalty associated with molecular crowding can generate pressure on the anchoring surface (Hiergeist and Lipowsky, 1996; Lipowsky, 1995; Stachowiak et al., 2012). Experimental studies with synthetic polymers have confirmed that the pressures generated by these unstructured macromolecules are sufficient to deform flexible lipid membranes (Busch et al., 2015; Evans and Rawicz, 1997; Hansen et al., 2003; Kenworthy et al., 1995). However, whether biopolymers in the glycocalyx might regulate plasma membrane morphologies through a similar mechanism remains largely untested.

RESULTS

Glycocalyx Polymers and Membrane Morphology

Guided by the framework of polymer brush theory, we hypothesized that glycocalyx polymers may generate an entropic bending force to favor the formation of curved membrane structures. As a corollary to this hypothesis, we envisioned that emergent membrane structures could be tuned through rational manipulation of the glycocalyx.

To test these hypotheses, we evaluated a genetically encoded library of native, semi-synthetic, and rationally designed mucin polymers of varying size, backbone sequence, and membrane anchorage (Figure 1A). Polymers considered included the 42 native tandem repeats (TRs) of Mucin-1 (Muc1-42TR), the serine-and threonine-rich polymer domain of Podocalyxin (Podxl; S/T-Rich), and a new synthetic mucin that we rationally designed based on a consensus mucin *O*-glycosylation sequence, PPASTSAPGA (Rational) (Figure 1A).

Each polymer domain was fused to the native Muc1 transmembrane anchor with the cytoplasmic tail deleted (ΔCT) or the native mucin transmembrane anchor with a membrane-proximal green fluorescent protein for imaging (GFP-ΔCT; Figure 1A). The cytoplasmic tails of the native membrane anchors were deleted to limit intracellular signal transduction by the mucins. We also created mucin chimeras with a synthetic 21-amino-acid transmembrane domain (TM21) to rule out that any observed effects of mucin expression could be attributed to the native mucin transmembrane domain and membrane-proximal sequences (Figure 1A). Each mucin expressed well on the cell surface (Figures S1A–S1C). The mucin polymer backbones were heavily glycosylated with *O*-linked sugar side chains to form the bottlebrush molecular structures that define mucins (Figures S1B and S1C).

When expressed at high levels on the epithelial cell surface, each of the long-chain mucins triggered a dramatic tubularization of the plasma membrane (Figures 1B and 1C). The phenotype was observed whether the mucin polymers were tethered to the membrane by a native-mucin transmembrane domain or synthetic membrane anchor (Figures 1B and 1C; compare

Figure 1. Flexible Glycocalyx Polymers Induce Membrane Projections

(A) The native and synthetic mucin biopolymers that were genetically encoded and used throughout this work.

(B) Quantification of membrane tube density in epithelial cells. Mucin polymers induce dramatic tubularization compared to wild-type (Control) cells and compared to a similarly sized biopolymer composed of EGF-like repeats from Notch1 and the Muc1 transmembrane anchor with GFP reporter (EGF-repeats GFP- Δ CT) cells. Number of cells analyzed is shown on the x axis for each condition. Box notches here and elsewhere indicate 95% confidence intervals. The number of tandem repeats (TRs) are indicated in Muc1 constructs.

(C) Scanning electron microscopy (SEM) images of cells expressing the indicated biopolymer.

(D) Labelled glycans and membrane morphologies resolved with single-molecule localization microscopy in Muc1-42TR ΔCT-expressing cells before and after mucin backbone digestion with the StcE mucinase. Images are shown as 2D color-coded histograms of localizations with 32 nm bin width.

(E) Representative confocal images of GUVs with and without anchorage of recombinant Podocalyxin.

(F) (Left) Cartoons of Muc1 GFP- Δ CT polymers of varying length. (Right) Flow cytometry data showing similar cell-surface expression levels of the mucins using a GFP-binding nanobody, n = 3, >40,000 cells per population.

(G) Representative SEM images of cells expressing mucins with a varying number of TRs.

(H) Quantification of membrane tube density for cells expressing the indicated mucins, significance compared to 42TR.

***p < 0.001; ns, not significant (*post-hoc* Student's two-tailed t test). See also Figure S1.

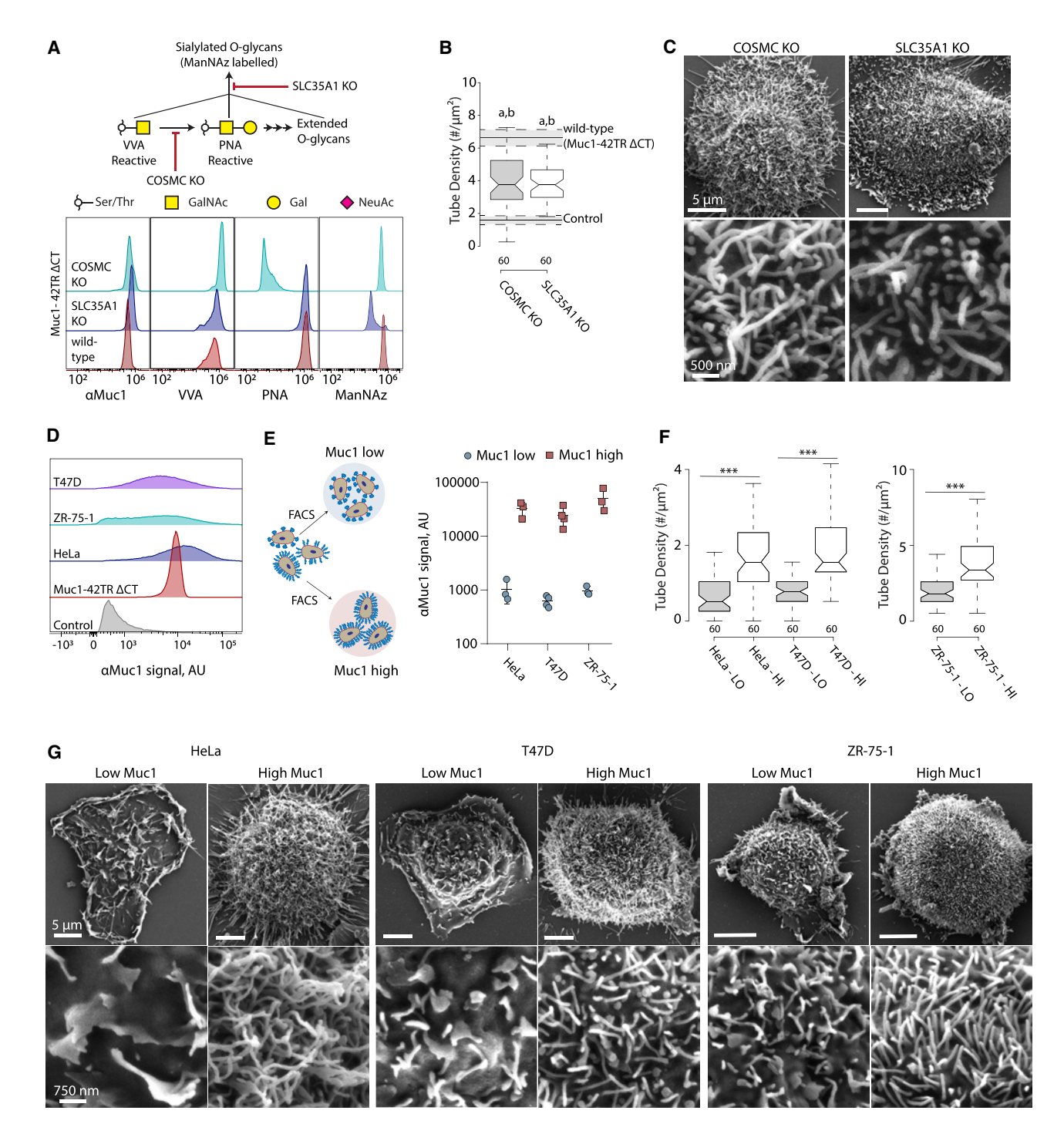


Figure 2. Mucin Polymer Expression Levels Predict Tumor Cell Morphologies

(A) (Upper) Illustration of expected effect of COSMC and SLC35A1 knockout (KO) on mucin O-glycan extension, sialylation, and lectin reactivity. (Lower) Flow cytometry data showing mucin levels, lectin reactivity, and sialylation (ManNAz labelling) of wild-type, COSMC KO, and SLC35A1 KO cells expressing Muc1-42TR Δ CT. (B) Quantification of membrane tube density on COSMC and SLC35A1 KO cells expressing Muc1-42TR Δ CT. For comparison, the mean tube density (dashed line region) and 95% confidence intervals (shaded area with dashed line regions) from Figure 1B are shown for wild-type cells (Control) and wild-type cells expressing Muc1-42TR Δ CT, significance compared to wild-type cells (Control) (a = p < 0.001), and significance compared to wild-type Muc1-42TR Δ CT-expressing cells (b = p < 0.001).

(C) SEM images showing the tubulated membrane morphologies of COSMC and SLC35A1 KO cells expressing Muc1-42TR Δ CT.

(D) Representative flow cytometry histograms showing endogenous Muc1 levels on the surface of various cancer cell lines and ectopic Muc1 levels on the surface of Muc1-42TR Δ CT-expressing cells, n = 3, >20,000 cells per population.

 Δ CT, GFP- Δ CT, and TM21). All of the mucin polymer domains were expected to be unstructured due to their high proline content and densely clustered serine and threonine sites for O-glycosylation. To test whether a more rigid, folded protein construct of comparable size to the mucins could induce a similar phenotype, we created a chimeric glycoprotein through fusion of the native Muc1 transmembrane anchor with repeating units of highly stable, epidermal growth factor (EGF)-like motifs from the ectodomain of human Notch1 (Kovall et al., 2017; Weisshuhn et al., 2016). The expressed Notch1 chimera was similar in molecular weight to fully glycosylated Muc1. However, the more rigid glycoprotein was largely ineffective at inducing membrane tubularization (Figures 1B, 1C, and S1B). We confirmed that the library of mucin constructs and chimeras were all expressed at similar levels on the cell surface, ruling out that the differences in membrane phenotype could be attributed to differential expression (Figure S1C).

We tested whether enzymatic digestion of the mucin-rich glycocalyx would destabilize the curved membrane features and revert tubularization. Glycans on live Muc1-42TR ΔCT-expressing cells were labeled and imaged with single-molecule localization microscopy (Möckl et al., 2018). The tubulated morphology of these cells was lost upon treatment with the specific mucinbackbone-digesting enzyme called secreted protease of C1 esterase inhibitor (StcE) from enterohemorrhagic E. coli (Malaker et al., 2018) (Figure 1D).

The rapid reversibility of the membrane morphologies following mucin digestion argued against excess membrane surface area as the underlying mechanism through which glycocalyx biopolymers exert control over cell-surface shapes. As an additional control, we conducted a standard transferrinreceptor internalization assay to evaluate the effects of mucin expression on endocytosis and recycling, which are key mechanisms of plasma-membrane area regulation in cells. We found that Muc1 expression did not have a significant effect on transferrin endocytosis (Figures S1D and S1E). We also found that mucin glycocalyx biopolymers could induce spontaneous curvature in model membrane systems that lack the machinery for active regulation of surface area and surface tension. Notably, the S/T-rich polymer domain of Podxl triggered extension of spherical and tubular membrane structures when anchored to the surface of giant unilamellar vesicles (GUVs) (Figures 1E and S1F).

The tubularization phenomenon observed in cells was relatively insensitive to the length of the mucin polymer domain, provided that the polymers were expressed on the cell surface at moderate to high densities. Cell lines expressing mucins with 0, 10, and 42 Muc1 TRs were sorted into populations with similar mucin surface densities (Figures 1F and S1G). Both 10- and 42-TR mucins induced significantly more plasma-membrane tubules than the construct lacking the repeats (Figures 1G and 1H). Comparison of cells with a similar spread area ruled out that effects associated with cell spreading could explain the morphological differences (Figure 1G).

Similar to our observations with mucins, we found that a glycocalyx rich in large, linear polysaccharides could also trigger dramatic changes in plasma-membrane morphology. Notably, hyaluronic acid synthase 3 (HAS3) expression increased the density of high-molecular-weight hyaluronic acid (HA) polymers on the cell surface and led to the protrusion of many finger-like membrane extensions (Figures S1H-S1K), consistent with prior observations (Koistinen et al., 2015). Together, these results suggested that diverse glycocalyx polymer types and sizes might influence cell morphological states.

Mucin Expression Predicts Tumor Cell Morphologies

Prior studies had found that the structural conformation of mucin biopolymers is largely determined by the initial αR-N-acetylgalactosamine (GalNAc) residues of the mucin O-glycans (Coltart et al., 2002). To confirm that more extended glycan structures were not required for membrane tubularization by mucins, we abrogated the extension of mucin O-glycan chains through CRISPR/Cas9-mediated knockout of Core-1 β3-T specific molecular chaperone (COSMC), which is required for elongation of the primary O-linked GalNAc monosaccharide into more complex Core O-glycans (Figure 2A) (Stolfa et al., 2016; Wang et al., 2010). We also targeted mucin sialylation through knockout of solute carrier family 35 member A1 (SLC35A1), which shuttles activated nucleotide sugars from the cytoplasm into the Golgi for sialic acid addition to glycans (Figure 2A) (Riemersma et al., 2015). The expected glycan perturbations were confirmed with flow cytometry using the Vicia villosa lectin (VVA) to probe non-extended α R-GalNAc, peanut agglutinin (PNA) to probe Core-1 glycans, and metabolic labelling with azide-functionalized sugars to detect sialic acid incorporation (Figure 2A). Disruption of O-glycan extension or sialylation did not block the strong induction of cell-surface tubularization by the Muc1 polymer backbone, although the density of membrane tubes on the cell surface was somewhat reduced compared to wild-type cells expressing the mucin at similar levels (Figures 2B and 2C).

Our results suggested that plasma-membrane morphologies might be predicted simply by the quantity of mucins or other biopolymers on the cell surface. We tested this possibility in carcinoma cell lines that are known to have abundant levels of Muc1 in their glycocalyx. In each tumor cell line tested—human breast cancer T47D, human breast cancer ZR-75-1, and human cervical HeLa-subpopulations were present that expressed endogenous Muc1 at comparable or higher levels than the ectopically expressed mucins evaluated earlier (Figures 1B, 1C, and 2D). Cells sorted for high Muc1 expression displayed significantly more tubules than cells expressing lower native levels of the mucins (Figures 2E, 2F, and 2G). Taken together, the results provided evidence that the well-known prevalence

⁽E) (Left) Strategy for sorting tumor cell lines into subpopulations with low and high surface levels of Muc1. (Right) Flow cytometry results confirming high and low surface levels on the sorted subpopulations; results presented as the geometric mean of the Muc1 signal across the indicated subpopulation.

⁽F) Quantification of membrane tube density on the sorted subpopulations.

⁽G) SEM images showing typical membrane morphologies in each sorted subpopulation.

^{***}p < 0.001 (post-hoc Student's two-tailed t test).

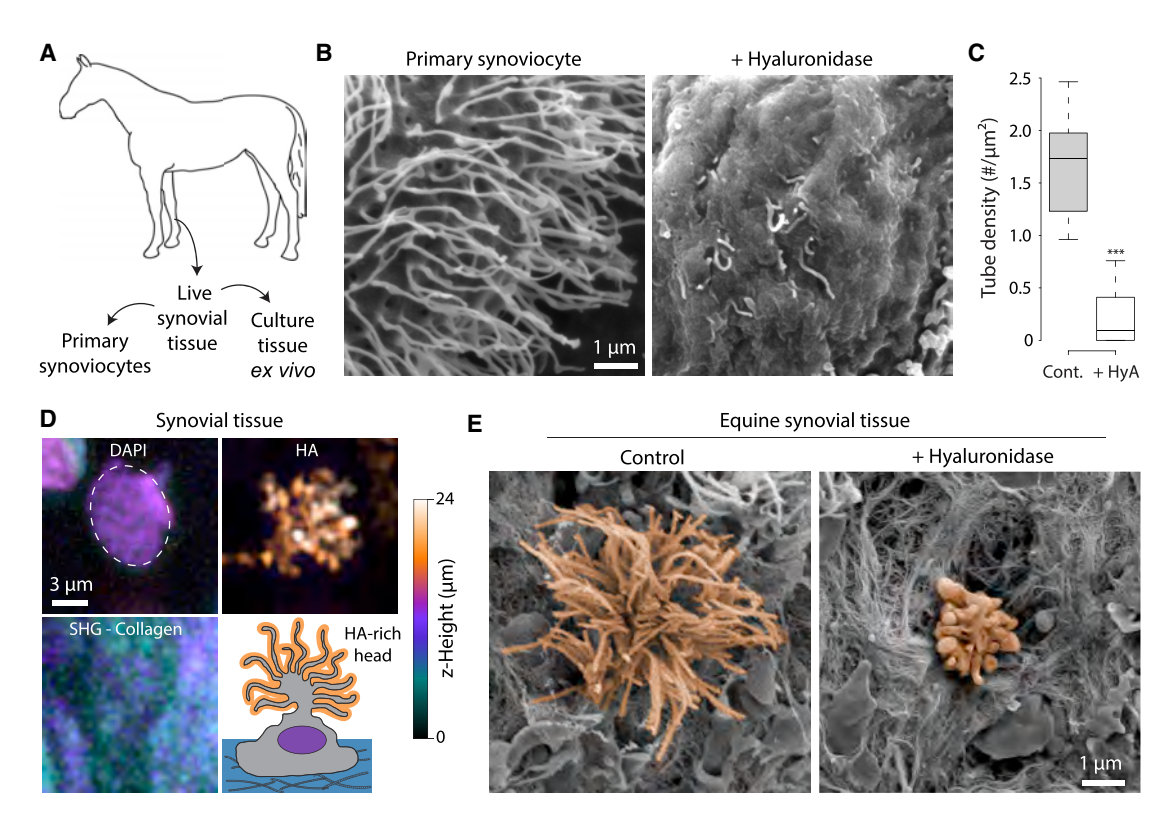


Figure 3. Membrane Morphology of Tissue Synoviocytes Is Regulated by the Glycocalyx

- (A) Experimental workflow for resected equine synovial tissues.
- (B) Representative SEM images of hyaluronic acid synthase 3 (HAS3)-expressing primary synoviocytes showing retraction of membrane tubules following 30 min of hyaluronidase (HyA) treatment to digest hyaluronic acid (HA).
- (C) Quantification showing tubule density was dependent on the presence of HA.
- (D) Images of freshly resected synovial tissue showing the nucleus (DAPI), surface-anchored HA (hyaluronic acid binding protein, HABP) of a representative synoviocyte, and the tissue collagen (second harmonic generation, SHG). Depth along the z axis is coded according to the color bar. Note the HA-enriched membrane extensions protruding from the synovial tissue surface. Lower right panel shows a cartoon representation of the observed tissue synoviocyte.
- (E) SEM images of freshly excised equine synovial tissue showing that the highly tubulated synoviocyte head, pseudo-colored in orange, is retracted after HyA treatment.

of tubulated features on tumor cells may be linked to their glyco-calyx (Kolata, 1975).

Specialized Cells In Vivo

Motivated by our observations in vitro, we considered whether glycocalyx polymers might play a role in shaping the morphology of specialized cell types in vivo. We elected to evaluate synoviocytes, because these secretory cells are known to produce large quantities of HA for joint lubrication and, thus, are expected to display a high density of HA polymers on their surface. We isolated synovial tissues from equine carpus (Figure 3A) and found that primary synoviocytes expressing HAS3 were highly tubulated, but treatment with hyaluronidase (HyA) to degrade HA resulted in the rapid destabilization and disappearance of membrane tubules (Figures 3B and 3C). We also evaluated synoviocyte morphology in tissues that were freshly extracted and briefly cultured ex vivo (<1 h). The synoviocytes in native synovial tissue displayed an HA-rich head that appeared highly tubulated and protruded from the tissue matrix (Figures 3D and 3E). Brief treatment of the tissue with HyA ex vivo resulted in a dramatic

retraction of synoviocyte tubules, suggesting a role for the glycocalyx in the maintenance of membrane projections *in vivo* (Figure 3E).

Polymer Brush Framework

To develop a more comprehensive understanding of membrane-shape regulation by glycocalyx polymers, we considered whether the observed membrane shapes and their frequencies could be rationalized through the framework of polymer brush theory. We noted that two limiting regimes are classically described in polymer physics for end-grafted polymers: the "mushroom" regime, where polymers at low grafting densities have limited interactions with each other, and the "brush" regime, where crowded polymers can interact sterically and electrostatically with each other to exert larger pressures on the anchoring surface (Milner, 1991) (Figure 4A). For mucins, we expected the transition from the mushroom to brush regime to occur at a surface density where the average distance between the polymers was approximately two times their radius of gyration in solution (Figure 4A).

^{***}p < 0.001 (post-hoc Student's two-tailed t test).

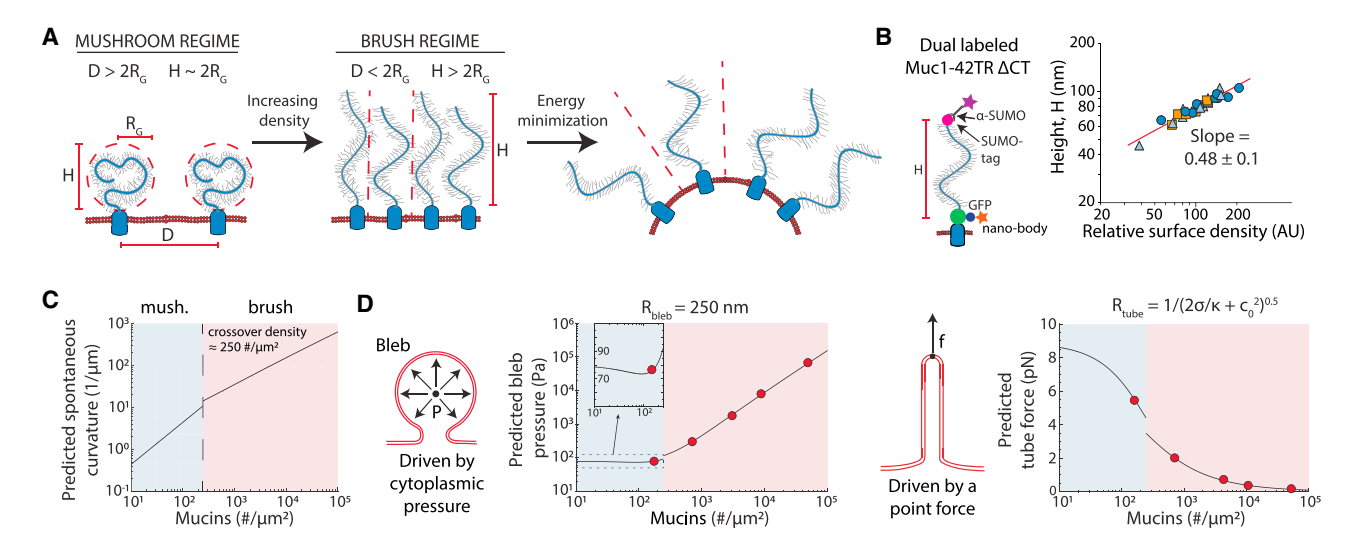


Figure 4. Polymer Brush Model of the Glycocalyx and Generation of Preferred Membrane Shapes

(A) Polymer model of membrane bending illustrating proposed spontaneous membrane curvature induced by the cellular glycocalyx. Low-density polymers are non-interacting and adopt a compact structure in the "mushroom" regime. In the "brush" regime, polymers overlap (the average distance between polymers, D, is less than the twice the radius of gyration, R_G) and extend to avoid each other, increasing the height of the polymer brush (H).

(B) (Left) Muc1 construct with SUMO and GFP tags flanking the polymer domain for visualization of polymer extension with expansion microscopy (ExM). (Right) Polymer extension versus polymer fluorescence intensity, a proportional measure of surface density, showing the indicated scaling relation. Dots, squares, and triangles indicate measurements from three samples. The red line shows a linear regression through all data points.

(C) Theoretical prediction of spontaneous curvature generation by Muc1 polymer mushrooms and polymer brushes. Blue, estimated mushroom regime (mush.); pink, estimated brush regime (brush). Based on experimental characterization, the computational model considers mucins of length 270 nm having monomeric seaments of length 15 nm (Kuhn length).

(D) (Left) Theoretical prediction of required pressure (Pa) as a function of mucin concentration for blebs of radii = 250 nm. The insert shows a pressure minimum near the mushroom-brush transition. (Right) Theoretical prediction of the required point force (pN) as a function of mucin concentration for maintaining membrane tubules

See also Figures S2 and S3.

To measure the radius of gyration and flexibility of individual mucins, we produced recombinant Muc1-42TR with a terminal purification tag in place of its transmembrane anchor (Figures S2A and S2B). Size-exclusion chromatography coupled to multi-angle light scattering (SEC-MALS) reported 32 nm ± 0.4% for the mucin radius of gyration in physiological buffer. Based on the estimated Muc1-42TR contour length of approximately 270 nm, we concluded that the mucin had a persistence length of approximately 7.5 nm and adopted the extended random coil configuration expected for a semi-flexible polymer in solution.

We next asked whether polymer brush theory could capture the physical behavior of mucin ensembles on the cell surface. We tested whether mucins stretch and extend in a predictable manner as they become progressively more crowded, a classic physical behavior predicted for polymer brushes (Alexander, 1977; de Gennes, 1980; Milner, 1991). We chose to evaluate mucin extension on actin-containing tubules that resembled microvilli, because the curvature of these structures was highly uniform and essentially independent of the mucin surface density due to the rigid actin cores (Figure S2C). As such, we could approximate the tubule surface as a rigid cylinder of fixed radius for direct comparison to theory. Epitope tags flanking the mucin polymer domain were introduced on Muc1-42TR. Following cellular expression, the encoded tags were labeled with fluorophore-conjugated probes and resolved on microvilli cross-sections using a super-resolution optical technique called expansion microscopy (ExM) (Figures 4B and S2D-S2F). We found that the mucin extension had an exponential dependence, or "scaled." with fluorescence intensity and, hence, surface density, with an exponent of 0.48 \pm 0.10 (Figure 4B). This value compared well to the theoretically derived power law exponent of between 0.33 and 0.5 for polyelectrolytes grafted on a rigid cylindrical surface at physiological salt concentrations (Zhulina and Borisov, 1996).

Encouraged by these findings, we created a polymer brush model to describe the physical behavior of a mucin-rich glycocalyx assembled on the plasma membrane (see STAR Methods). In our model, entropic pressure from the mucin brush generated spontaneous membrane curvature that scaled strongly with polymer density and weakly with polymer chain length (Hiergeist and Lipowsky, 1996) (Figures 4C and S3). The weak dependence on polymer length was consistent with our earlier findings that mucins with 10 and 42 repeats had comparable effects on cellsurface morphology despite their 4-fold difference in size (Figures 1G, 1H, and S1G). For 10 and 42 TR mucins, our brush model predicted only a ~20% difference in spontaneous membrane curvature (Figure S3).

Preferred Membrane Shapes

We tested whether the polymer model could explain the frequency of finger-like and spherical protrusions from the cell

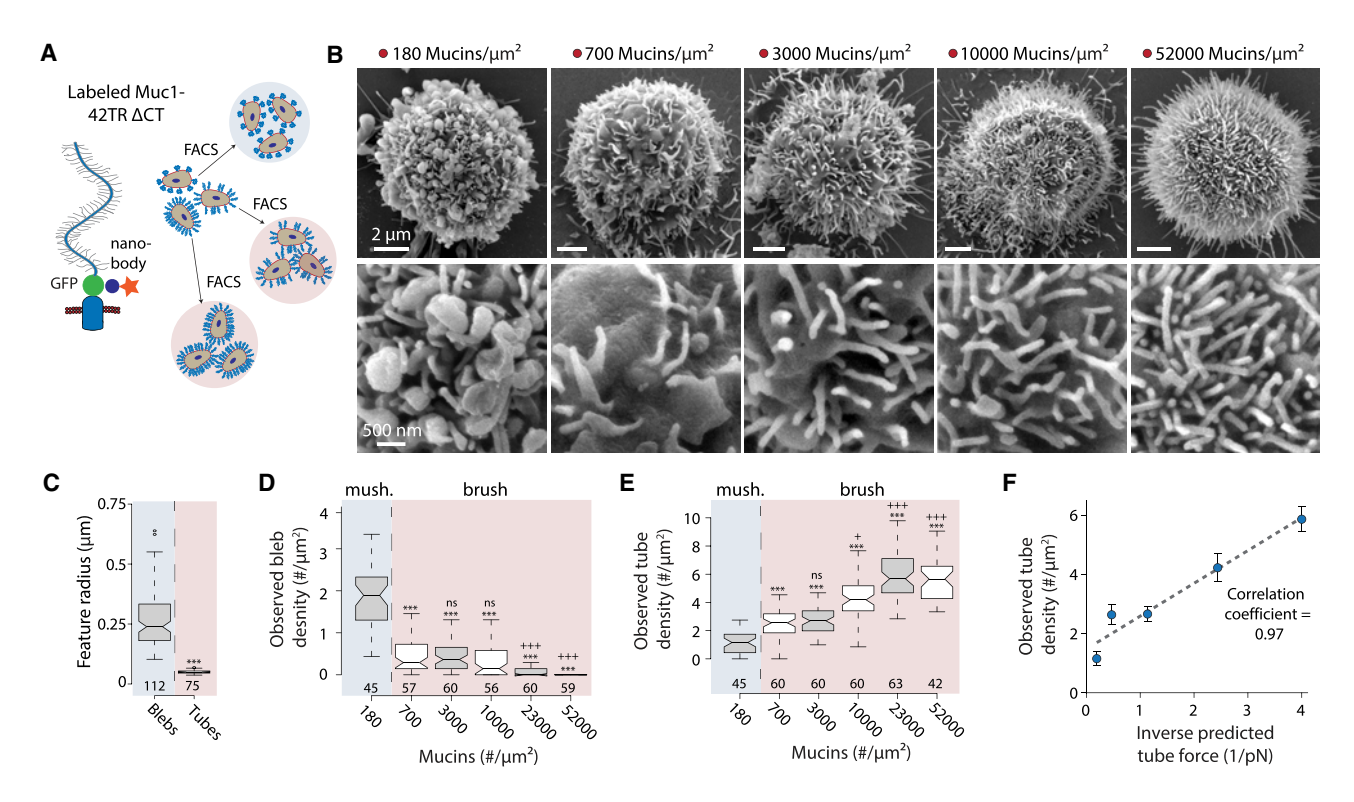


Figure 5. Preferred Membrane Shape Depends on Cell-Surface Biopolymer Concentrations

- (A) Strategy for sorting cells into populations with varying levels of cell-surface mucin (Muc1-42TR-GFP Δ CT) using fluorescence-activated cell sorting (FACS). (B) Representative SEM images showing the transition of membrane morphological features of sorted cell populations with the indicated mucin surface density. Mucin densities were chosen to match the indicated points on the theoretical graphs (Figure 4D).
- (C) Average radius of bleb structures measured in the mushroom regime and tube structures measured in the brush regime.
- (D) Observed density of membrane blebs on sorted cell populations having the indicated average mucin surface density. Significance was determined between mushroom regime and brush regime (*) or between the lowest brush-regime density and all other brush mucin densities (+).
- (E) Observed density of membrane tubes on sorted cell populations having the indicated average mucin surface density. Symbols defined in (D).
- (F) Inverse predicted force from Figure 4D, right, versus the observed tube density from (E) exhibits a linear relationship and Pearson correlation coefficient of 0.97. Number of measurements shown on the x axis of boxplots. Error bars indicate 95% confidence intervals. ns, not significant; */+p < 0.05; **/++p < 0.01; ***/+++p < 0.001 (post-hoc Student's two-tailed t test).

See also Figure S4.

surface. We reasoned that protrusion of a specific membrane feature would be disfavored when high intracellular forces were required to extend or maintain the protrusion and favored when these force requirements were minimal. Minimizing the standard Helfrich free-energy function for membranes with induced spontaneous curvature, we calculated the equilibrium cytosolic pressure required to maintain a spherical membrane bleb and the point force required to maintain a membrane tubule (Derényi et al., 2002) (Figure 4D; see STAR Methods). For experimental comparison, we evaluated the types, sizes, and frequencies of plasma-membrane features as a function of mucin cell-surface density. Cells expressing Muc1-42TR GFP Δ CT were labeled with an anti-GFP nanobody and sorted into populations of varying mucin surface levels (Figures 5A and 5B). The average mucin surface density in each population was estimated by SDS-PAGE through interpolation using a nanobody standard curve (Figure S4). Molecular surface densities in the sorted populations ranged from approximately 180 to 50,000 mucins per μm². For reference, we expected the mushroom-to-brush transition to occur around 250 mucins

per μm^2 based on the measured radius of gyration of recombinant Muc1-42TR in solution.

Initially, we evaluated membrane blebs. Using physical parameters measured for Muc1-42TR, we predicted that the pressure required for maintaining a bleb with a typical radius of 250 nm would be minimal at moderate mucin densities near the mushroom-brush transition (Figures 5C and 5D). An important model prediction was that the required maintenance pressure would rise sharply at higher mucin densities, quickly reaching pressures that exceed the known limits of the cell's contractile machinery (Charras et al., 2008). Thus, theory suggested that blebbing would be supported by low mucin densities and suppressed by a highly dense glycocalyx (Figure 4D). Our experimental observations showed good qualitative agreement with these predictions. Cells with a mucin density near the estimated mushroom-brush transition displayed a significant number of large, bleb-like forms with an average radius of 260 \pm 100 nm (Figures 5B-5D; 180 mucins per μ m²). Upon crossover into the brush regime, the bleb frequency plummeted precipitously, consistent with the model's prediction of a quadratic rise in the necessary bleb maintenance pressure (Figures 5B–5D).

The glycocalyx polymer model predicted a much different dependence of membrane tubule extension on mucin density. The predicted point force required for maintaining an extended tubule decreased progressively with high mucin densities and exhibited no sharp transitions (Figure 4D). Accordingly, the frequency of cell-surface tubules observed in our sorted cell populations increased steadily with mucin density throughout the mushroom and brush regimes until the cell was fully saturated with tubes at very high mucin densities (Figures 5B-5E). Notably, theory predicted that at these high densities, the required force for tubule extension is comparable to the polymerization force of a single cytoskeletal filament, ~1 pN (Footer et al., 2007). Based on the experimentally measured mucin densities, we estimated the theoretical point force, f, required to maintain tubules. Remarkably, the experimentally observed tube frequency on our sorted cell populations had a nearly perfect inverse correlation with the theoretical point force calculated for the corresponding mucin density (Figure 5F). The Pearson's correlation coefficient describing the relationship between tube density and 1/f was 0.97.

Membrane Instabilities and Microvesicle Generation

We next considered whether other functional membrane shapes could be generated through actions of the glycocalyx. We noted that the tubular membrane projections on our cells typically contained a filamentous actin (F-actin) core and did not contain microtubules (Figures 6A, 6B, and S5A–S5D). Disruption of F-actin assembly with the drug Latrunculin A (LatA) led to a reduction in tubule diameter by approximately 30 nm (Figures 6C, 6D, S5E, and S5F), indicating that the mucin-induced spontaneous curvature exceeded the curvature of the stable, actin-filled projections. Notably, LatA treatment triggered the formation of pearled and undulating structures that characteristically arise through membrane instabilities (Bar-Ziv et al., 1999) (Figure 6D).

Deuling, Helfrich, and others theoretically considered instabilities in membrane tubules with volume to area ratio, λ , and found that for certain spontaneous curvatures, c_0 , the membrane bending energy vanished through the adoption of one of three "Delaunay" shapes: a cylinder for $c_0 = 1/2\lambda$ (Shape 1), a smoothly varying set of unduloids for $1/2\lambda < c_0 < 2/3\lambda$ (Shape 2), and a set of equal-sized "pearls" for $c_0 = 2/3\lambda$ (Shape 3) (Campelo and Hernández-Machado, 2007; Tsafrir et al., 2001). For spontaneous curvatures that exceeded 2/3\u03b1, the lowest energy shapes that satisfied the constraints of volume and surface area were found to include a set of small pearls of the preferred curvature with one or more big pearls necessary to hold excess volume (Shape 4) or a set of pearls with a gradient in size (Shape 5) (Campelo and Hernández-Machado, 2007; Tsafrir et al., 2001). We evaluated whether the minimal energy surfaces, Shapes 1 to 5, would be formed on cells expressing moderate to high levels of mucin without exogenous treatments and found commonplace examples of each expected minimal energy shape (Figure 6E). The pearled structures were not observed in control cells that did not express high levels of mucin.

Previous theoretical and experimental studies indicated that the thin membrane necks connecting pearled membrane struc-

tures, such as those observed on our cells, would be expected to undergo spontaneous fissure due to the high elastic stress accumulated in the constricted necks (Kozlovsky and Kozlov, 2003; Morlot et al., 2012; Snead et al., 2017). Therefore, we hypothesized that microvesicles would be released as a consequence of the mucin-induced membrane instabilities (Figure 6F). We found that the conditioned media from Muc1-42TR-expressing cells contained massive concentrations of particles ranging in size from approximately 100 nm to 400 nm (Figure 6G). Particle generation was further enhanced by LatA treatments that disrupted the supporting F-actin cores of surface projections (Figures 6H and S5F). Cryo-transmission electron microscopy (cryo-TEM) confirmed that the secreted particles were membrane vesicles grafted with a distinct glycocalyx ultrastructure on their surfaces (Figure 6I). The removal of the glycocalyx, such as by HyA treatment to remove HA from the cell surface of HAS3-expressing cells, significantly reduced vesicle production (Figure 6J).

High numbers of microvesicle generation have been reported in many cancer-cell types (Menck et al., 2017; Muralidharan-Chari et al., 2010). We tested whether high mucin expression, which is common in tumor cells, might at least partially explain why these cells have a propensity to generate microvesicles. We found that HeLa tumor-cell subpopulations sorted for high endogenous Muc1 expression produced significantly more vesicles than cell populations with low endogenous Muc1 levels (Figure 6K).

Together, our results suggested a possible sequence for microvesicle generation: (1) the glycocalyx enables cytoskeletal filaments to extend and stabilize thin protrusions from the plasma membrane, and (2) after disassembly of the cytoskeletal core, spontaneous curvature imposed by the glycocalyx induces formation of membrane pearls that spontaneously fissure to release vesicles (Figures 6E and 6F).

DISCUSSION

Overall, the theories and experiments presented here implicate an entropic mechanism through which the glycocalyx can strongly influence the favorability of diverse plasma membrane shapes and protrusions. The morphological changes regulated by the glycocalyx could, in principle, have broad consequences on membrane processes, ranging from absorption and secretion to cellular communication, signaling, and motility (Lange, 2011; Paluch and Raz, 2013; Sauvanet et al., 2015; Schmick and Bastiaens, 2014). Given that glycosylation often changes dramatically with cell-fate transitions (Buck et al., 1971; Freeze, 2013; Satomaa et al., 2009) and that the pool of monomers for construction of glycoproteins and glycosaminoglycans in the glycocalyx is tightly coupled to specific metabolic programs (Dennis et al., 2009; Koistinen et al., 2015; Ying et al., 2012), our work raises the intriguing possibility that the glycocalyx may serve as a conduit linking physical morphology to specific cell states.

Contemporary frameworks for understanding membrane-shape regulation largely lack a physical description of the glycocalyx. However, long-chain biopolymers in the glycocalyx are almost universally found anchored to the surfaces of curved membrane features and cell-surface organelles (Bennett et al., 2001; Button et al., 2012; Fowke et al., 2017; Hattrup and Gendler, 2008; Kesavan et al., 2009; Kesimer et al., 2013; Makabe

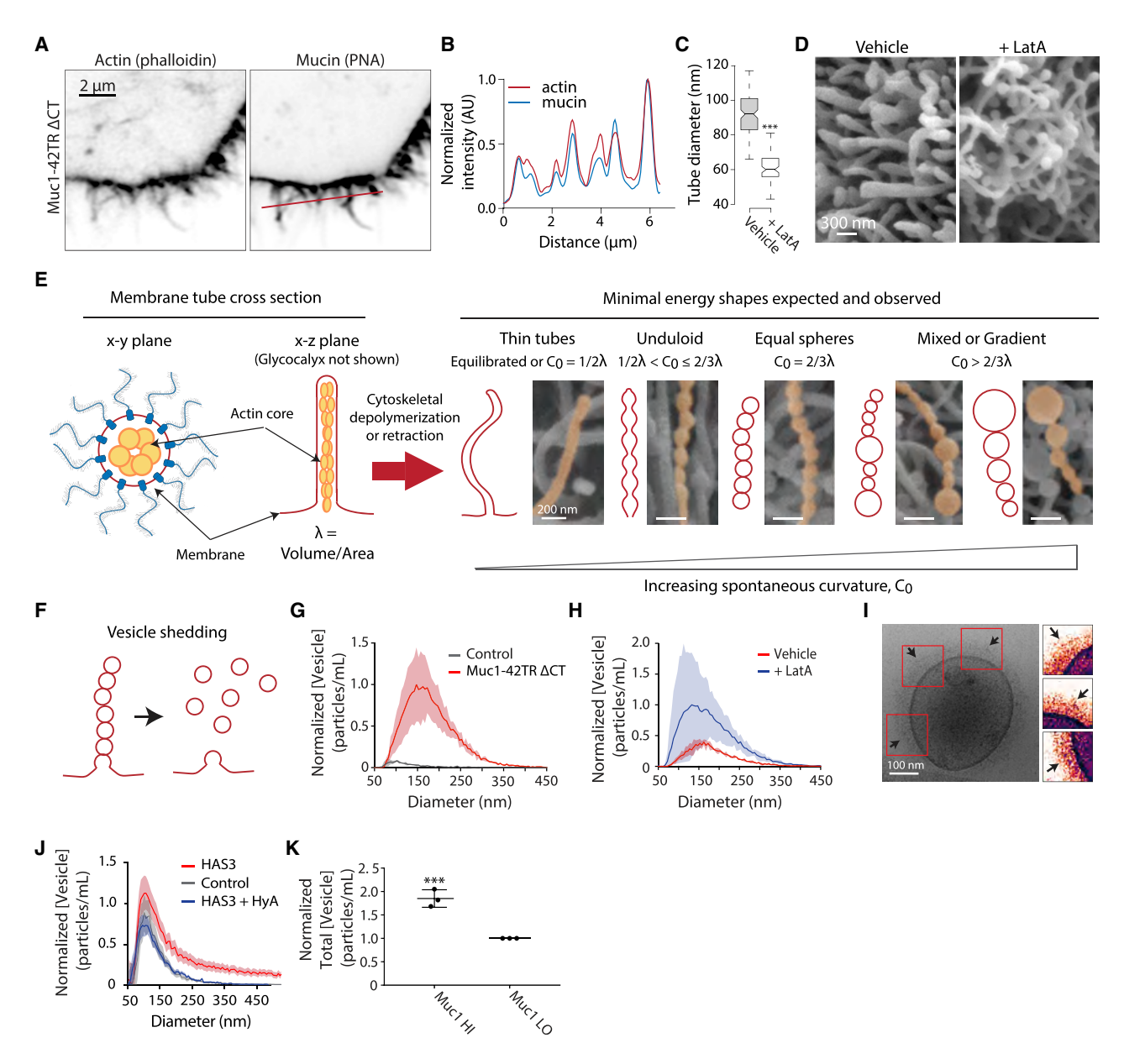


Figure 6. Glycocalyx-Mediated Membrane Instabilities and Microvesicle Biogenesis

(A) Representative confocal microscopy images of epithelial cells expressing Muc1-42TR Δ CT and stained with PNA (peanut agglutinin) for mucins and phalloidin for actin, n = 3.

- (B) Fluorescent intensity line trace from (A) (PNA image, red line). Values are normalized for their respective maximum intensities for phalloidin and PNA stains. (C) Average diameter of tubules in Muc1-42TR ΔCT-expressing cells following treatment with DMSO (Vehicle) or with 10 μM Latrunculin-A (+ LatA) to disrupt actin assembly.
- (D) Representative SEM images of tubules in vehicle-treated or LatA-treated cells expressing Muc1-42TR Δ CT.
- (E) (Left) Cartoon schematic of a proposed model in which the actin core resists the spontaneous membrane curvature driven by the glycocalyx brush. Upon actin depolymerization, membrane tubules are destabilized and predicted to relax into (right) various pearled structures and/or thin tubes that represent minimal energy surfaces. Schematic drawings of these predictions are shown alongside representative pseudo-colored SEM images showing examples of the structures in cells expressing Muc1-42TR ΔCT.
- (F) Cartoon schematic of proposed mechanism whereby pearled structures vesiculate.
- (G) Histogram showing the average concentration and size distribution of extracellular vesicles for wild-type (Control) and Muc1-42TR ΔCT-expressing cells. Shaded area shows the 95% confidence interval for all histograms.
- (H) Histogram showing the average concentration and size distribution of extracellular vesicles for Muc1-42TR ΔCT cells treated with DMSO (Vehicle) or LatA (+ LatA), n = 5, 5, 4, 7, respectively.
- (I) Representative cryogenic transmission electron microscopy (cryo-TEM) image of a vesicle collected from cells expressing Muc1-42TR Δ CT. Red boxes indicate pseudo-colored regions of interest shown on the right.

(legend continued on next page)

et al., 2006; van den Pol and Kim, 1993; Zhang et al., 1992). Our results suggest that the principles and theories of polymer physics can be adopted to understand, at least to a first approximation, the physical regulation of membrane-shape generation by the glycocalyx. Undoubtedly, a model of end-anchored polymer mushrooms and polymer brushes is a simple physical representation of the glycocalyx. However, the inverse relationship between the force requirements for membrane extension, as estimated using a relatively simple model of the glycocalyx, and the experimentally observed frequencies of these extensions argue that at least some of the physical behaviors of the glycocalyx can be captured using well-established polymer models (de Gennes, 1979; Zhulina and Borisov, 1996).

Our model and analyses assume constant membrane tension, leading to the prediction that the lengths of tubular projections are invariant of force. In reality, cells have a finite reservoir of membrane (Raucher and Sheetz, 1999). Increasing membrane tension after depletion of reservoirs would ultimately limit the length of tubular forms projected from the membrane (Cuvelier et al., 2005; Raucher and Sheetz, 1999). Transport limitations of cytoskeletal monomers also likely place an important constraint limiting the overall length of long and thin membrane projections (Mogilner and Rubinstein, 2005). Indeed, we only report a weak dependence of tubule length on glycocalyx polymer density (Figure 5B).

Bending of surfaces by anchored polymers is a general physical phenomenon (Busch et al., 2015; Evans and Rawicz, 1997; Hansen et al., 2003; Hiergeist and Lipowsky, 1996; Kenworthy et al., 1995; Lipowsky, 1995; Stachowiak et al., 2012). As such, membrane-shape regulation by the glycocalyx could be a universal feature in the biogenesis of curved membrane organelles and signaling structures. For instance, cilia, axons, cytonemes, tunneling nanotubes, microvilli, and microvesicles could all conceivably be regulated by physical forces related to the glycocalyx. Thus, our work argues for a more holistic model of membrane-shape regulation that includes consideration of forces on both the intracellular and extracellular faces of the plasma membrane.

STAR*METHODS

Detailed methods are provided in the online version of this paper and include the following:

- KEY RESOURCES TABLE
- CONTACT FOR REAGENT AND RESOURCE SHARING
- EXPERIMENTAL MODEL AND SUBJECT DETAILS
 - Cell Lines
 - Primary Synoviocyte Isolation and Culture
 - O Equine Synovial Tissue Resection

METHOD DETAILS

- Cloning and Constructs
- O Immuno- and Lectin Blot Analysis
- O Flow Cytometric Analysis
- Confocal Microscopy for Cells and Tissues
- Scanning Electron Microscopy
- Mucin Digestion and Super-Resolution Imaging
- Giant Unilamellar Vesicles
- Endocytosis Assay
- Analysis of HA Synthesis
- Analysis of HA Molecular Size
- Cancer Cell Line Sorting
- Analysis of Mucin Radius of Gyration
- O Variation of Mucin Size and Surface Densities
- Expansion Microscopy
- Isolation of Extracellular Vesicles
- Plunge-Freezing Vitrification
- Cryogenic Transmission Electron Microscopy
- O Theoretical Model Details

QUANTIFICATION AND STATISTICAL ANALYSIS

- Scanning Electron Microscopy Quantification
- Giant Unilamellar Vesicles Quantification
- Nanoparticle Tracking Analysis
- O Expansion Microscopy Quantification
- Statistics
- DATA AND SOFTWARE AVAILABILITY

ACKNOWLEDGMENTS

We acknowledge the Woods Hole Cell Physiology Course and its participants for assistance with preliminary investigations. We thank J. Lakins and V. Weaver for empty lentiviral and transposon plasmids; B. Peal for assistance in harvesting synovial tissues; and A. Stroock, L. Archer, J. Lammerding, C. Fischbach, and D. Koch for helpful discussions. This investigation was supported by the National Institute of General Medical Sciences (NIGMS) 2T32GM008267 (C.R.S., M.J.C.), Knight Family Foundation Graduate Research Fellowship (C.R.S.), Samuel C. Fleming Family Graduate Fellowship (C.R.S.), National Science Foundation (NSF) Graduate Research Fellowship (M.J.C., L.M.R., and K.P.), Ford Foundation Predoctoral Fellowship (L.M.R.), Stanford Graduate Fellowship (K.P.), Stanford ChEM-H Chemistry/Biology Interface Predoctoral Training Program (K.P.), NIGMS R37GM058867 (C.R.B.), National Cancer Institute (NCI) R01CA227942 (C.R.B.), NIGMS R35GM118067 (W.E.M.), National Institute of Health (NIH) New Innovator DP2 GM229133 (M.J.P.), and NCI U54 CA210184 (M.J.P.). This work made use of the Cornell Center for Materials Research Shared Facilities (NSF DMR-1719875), the Cornell Nanoscale Science and Technology Facility (NSF ECCS-1542081), and the Cornell Biotechnology Resource Center Imaging Facility (NIH S100D018516).

AUTHOR CONTRIBUTIONS

All authors contributed to the design of the studies and preparation of the manuscript. C.R.S., L.M.R., H.P., J.S., and M.J.P. constructed plasmids. C.R.S., J.C.-H.K., L.M.R., and M.J.C. conducted fluorescence and scanning

⁽J) Representative histogram showing average concentration and size distribution of extracellular vesicles for wild-type (Control), hyaluronic acid synthase 3 (HAS3)-expressing human mammary epithelial cells, and HAS3-expressing cells treated with hyaluronidase (HyA). Particle concentration is normalized to the max peak for each graph, n = 4, 5, 3, respectively.

⁽K) Average concentration of extracellular vesicles from HeLa cells sorted for high or low Muc1 surface levels. Results represent the sum of all vesicles, independent of size, n = 3.

^{**}p < 0.001 (post hoc two-tailed Student's t test). See also Figure S5.

electron microscopy. C.R.S. and L.M.R. conducted flow cytometry and cell sorting. L.M.R., R.Y., and M.J.H. analyzed microvesicles. T.A.E. conducted GUV experiments. J.M.N. conducted cryogenic electron microscopy. K.P. prepared StcE-digested samples and L.M. conducted localization microscopy and analysis. C.R.S. produced recombinant Muc1 and J.P.O performed SEC-MALS. J.G.G. and M.J.P. constructed the model. H.L.R. harvested equine synovial tissue. J.S. and H.L.R. prepared equine synoviocytes.

DECLARATION OF INTERESTS

A patent application relating to the use of StcE mucinase has been filed by Stanford University (docket number STAN-1510PRV). C.R.B. is a co-founder and Scientific Advisory Board member of Palleon Pharmaceuticals, Enable Bioscience, Redwood Biosciences, and InterVenn Biosciences and a member of the Board of Directors of Eli Lilly & Company.

Received: August 2, 2018 Revised: February 19, 2019 Accepted: April 9, 2019 Published: May 2, 2019

REFERENCES

Agrawal, B., Krantz, M.J., Parker, J., and Longenecker, B.M. (1998). Expression of MUC1 mucin on activated human T cells: implications for a role of MUC1 in normal immune regulation. Cancer Res. 58, 4079–4081.

Alexander, S. (1977). Adsorption of chain molecules with a polar head a scaling description. J. Phys. 38, 983–987.

Angelova, M.I., and Dimitrov, D.S. (1986). Liposome electroformation. Faraday Discuss. Chem. Soc. *81*, 303–311.

Antonyak, M.A., Li, B., Boroughs, L.K., Johnson, J.L., Druso, J.E., Bryant, K.L., Holowka, D.A., and Cerione, R.A. (2011). Cancer cell-derived microvesicles induce transformation by transferring tissue transglutaminase and fibronectin to recipient cells. Proc. Natl. Acad. Sci. USA *108*, 4852–4857.

Bäckström, M., Link, T., Olson, F.J., Karlsson, H., Graham, R., Picco, G., Burchell, J., Taylor-Papadimitriou, J., Noll, T., and Hansson, G.C. (2003). Recombinant MUC1 mucin with a breast cancer-like O-glycosylation produced in large amounts in Chinese-hamster ovary cells. Biochem. J. 376, 677–686.

Bar-Ziv, R., Tlusty, T., Moses, E., Safran, S.A., and Bershadsky, A. (1999). Pearling in cells: a clue to understanding cell shape. Proc. Natl. Acad. Sci. USA *96*, 10140–10145.

Becker, A., Thakur, B.K., Weiss, J.M., Kim, H.S., Peinado, H., and Lyden, D. (2016). Extracellular Vesicles in Cancer: Cell-to-Cell Mediators of Metastasis. Cancer Cell *30*, 836–848.

Bennett, R., Jr., Järvelä, T., Engelhardt, P., Kostamovaara, L., Sparks, P., Carpén, O., Turunen, O., and Vaheri, A. (2001). Mucin MUC1 is seen in cell surface protrusions together with ezrin in immunoelectron tomography and is concentrated at tips of filopodial protrusions in MCF-7 breast carcinoma cells. J. Histochem. Cytochem. 49, 67–77.

Bergert, M., Erzberger, A., Desai, R.A., Aspalter, I.M., Oates, A.C., Charras, G., Salbreux, G., and Paluch, E.K. (2015). Force transmission during adhesion-in-dependent migration. Nat. Cell Biol. *17*, 524–529.

Bischoff, M., Gradilla, A.-C., Seijo, I., Andrés, G., Rodríguez-Navas, C., González-Méndez, L., and Guerrero, I. (2013). Cytonemes are required for the establishment of a normal Hedgehog morphogen gradient in *Drosophila* epithelia. Nat. Cell Biol. *15*, 1269–1281.

Borisov, O.V., and Zhulina, E.B. (2002). Effect of Salt on Self-Assembly in Charged Block Copolymer Micelles. Macromolecules *35*, 4472–4480.

Bracha, D., Karzbrun, E., Shemer, G., Pincus, P.A., and Bar-Ziv, R.H. (2013). Entropy-driven collective interactions in DNA brushes on a biochip. Proc. Natl. Acad. Sci. USA *110*. 4534–4538.

Bramwell, M.E., Wiseman, G., and Shotton, D.M. (1986). Electron-microscopic studies of the CA antigen, epitectin. J. Cell Sci. 86, 249–261.

Buck, C.A., Glick, M.C., and Warren, L. (1971). Glycopeptides from the surface of control and virus-transformed cells. Science 172, 169–171.

Busch, D.J., Houser, J.R., Hayden, C.C., Sherman, M.B., Lafer, E.M., and Stachowiak, J.C. (2015). Intrinsically disordered proteins drive membrane curvature. Nat. Commun. 6, 7875.

Button, B., Cai, L.-H., Ehre, C., Kesimer, M., Hill, D.B., Sheehan, J.K., Boucher, R.C., and Rubinstein, M. (2012). A periciliary brush promotes the lung health by separating the mucus layer from airway epithelia. Science *337*, 937–941.

Campelo, F., and Hernández-Machado, A. (2007). Model for curvature-driven pearling instability in membranes. Phys. Rev. Lett. 99, 088101.

Charras, G., and Paluch, E. (2008). Blebs lead the way: how to migrate without lamellipodia. Nat. Rev. Mol. Cell Biol. 9, 730–736.

Charras, G.T., Yarrow, J.C., Horton, M.A., Mahadevan, L., and Mitchison, T.J. (2005). Non-equilibration of hydrostatic pressure in blebbing cells. Nature *435*, 365–369

Charras, G.T., Coughlin, M., Mitchison, T.J., and Mahadevan, L. (2008). Life and times of a cellular bleb. Biophys. J. 94, 1836–1853.

Chen, W.L., Cordero, R., Tran, H., and Ober, C.K. (2017). 50th Anniversary Perspective: Polymer Brushes: Novel Surfaces for Future Materials. Macromolecules *50*, 4089–4113.

Cleland Robert, L. (2004). Viscometry and sedimentation equilibrium of partially hydrolyzed hyaluronate: Comparison with theoretical models of wormlike chains. Biopolymers 23, 647–666.

Cloosen, S., Thio, M., Vanclée, A., van Leeuwen, E.B., Senden-Gijsbers, B.L., Oving, E.B., Germeraad, W.T., and Bos, G.M. (2004). Mucin-1 is expressed on dendritic cells, both in vitro and in vivo. Int. Immunol. *16*, 1561–1571.

Coltart, D.M., Royyuru, A.K., Williams, L.J., Glunz, P.W., Sames, D., Kuduk, S.D., Schwarz, J.B., Chen, X.-T., Danishefsky, S.J., and Live, D.H. (2002). Principles of mucin architecture: structural studies on synthetic glycopeptides bearing clustered mono-, di-, tri-, and hexasaccharide glycodomains. J. Am. Chem. Soc. *124*, 9833–9844.

Costantini, L.M., Baloban, M., Markwardt, M.L., Rizzo, M., Guo, F., Verkhusha, V.V., and Snapp, E.L. (2015). A palette of fluorescent proteins optimized for diverse cellular environments. Nat Commun 6, 7670.

Cowman, M.K., Spagnoli, C., Kudasheva, D., Li, M., Dyal, A., Kanai, S., and Balazs, E.A. (2005). Extended, relaxed, and condensed conformations of hyaluronan observed by atomic force microscopy. Biophys. J. 88, 590–602.

Cuvelier, D., Chiaruttini, N., Bassereau, P., and Nassoy, P. (2005). Pulling long tubes from firmly adhered vesicles. Europhys. Lett. *71*, 1015–1021.

D'Aloia, M.M., Zizzari, I.G., Sacchetti, B., Pierelli, L., and Alimandi, M. (2018). CAR-T cells: the long and winding road to solid tumors. Cell Death Dis. 9, 282.

Day, A.J., and Sheehan, J.K. (2001). Hyaluronan: polysaccharide chaos to protein organisation. Curr. Opin. Struct. Biol. *11*, 617–622.

de Gennes, P. (1979). Scaling Concepts in Polymer Physics (Ithaca, NY: Cornell University Press).

de Gennes, P. (1980). Conformations of polymers attached to an interace. Macromolecules *13*, 1069–1075.

Dennis, J.W., Nabi, I.R., and Demetriou, M. (2009). Metabolism, cell surface organization, and disease. Cell *139*, 1229–1241.

Derényi, I., Jülicher, F., and Prost, J. (2002). Formation and interaction of membrane tubes. Phys. Rev. Lett. 88, 238101.

Evanko, S.P., Tammi, M.I., Tammi, R.H., and Wight, T.N. (2007). Hyaluronan-dependent pericellular matrix. Adv. Drug Deliv. Rev. *59*, 1351–1365.

Evans, E., and Rawicz, W. (1997). Elasticity of "Fuzzy" Biomembranes. Phys. Rev. Lett. 79. 2379–2382.

Footer, M.J., Kerssemakers, J.W.J., Theriot, J.A., and Dogterom, M. (2007). Direct measurement of force generation by actin filament polymerization using an optical trap. Proc. Natl. Acad. Sci. USA *104*, 2181–2186.

Fowke, T.M., Karunasinghe, R.N., Bai, J.-Z., Jordan, S., Gunn, A.J., and Dean, J.M. (2017). Hyaluronan synthesis by developing cortical neurons *in vitro*. Sci. Rep. 7, 44135.

Freeze, H.H. (2013). Understanding human glycosylation disorders: biochemistry leads the charge. J. Biol. Chem. 288, 6936–6945.

Friedl, P., and Wolf, K. (2010). Plasticity of cell migration: a multiscale tuning model. J. Cell Biol. 188, 11–19.

Gangoda, L., Boukouris, S., Liem, M., Kalra, H., and Mathivanan, S. (2015). Extracellular vesicles including exosomes are mediators of signal transduction: are they protective or pathogenic? Proteomics *15*, 260–271.

Gupton, S.L., and Gertler, F.B. (2007). Filopodia: the fingers that do the walking. Sci. STKE 2007, re5.

Halpern, A.R., Howard, M.D., and Vaughan, J.C. (2015). Point by Point: An Introductory Guide to Sample Preparation for Single-Molecule, Super-Resolution Fluorescence Microscopy. Curr. Protoc. Chem. Biol. 7, 103–120.

Hansen, P.L., Cohen, J.A., Podgornik, R., and Parsegian, V.A. (2003). Osmotic properties of poly(ethylene glycols): quantitative features of brush and bulk scaling laws. Biophys. J. 84, 350–355.

Hattrup, C.L., and Gendler, S.J. (2008). Structure and function of the cell surface (tethered) mucins. Annu. Rev. Physiol. 70, 431–457.

Hayashi, K., Tsutsumi, K., Nakajima, F., Norisuye, T., and Teramoto, A. (1995). Chain-stiffness and excluded-volume effects in solutions of sodium hyaluronate at high ionic strength. Macromolecules *28*, 3824–3830.

Helfrich, W. (1973). Elastic properties of lipid bilayers: theory and possible experiments. Z. Naturforsch. C 28, 693–703.

Hiergeist, C., and Lipowsky, R. (1996). Elastic Properties of Polymer-Decorated Membranes. J. Phys. II 6, 1465–1481.

Hong, V., Steinmetz, N.F., Manchester, M., and Finn, M.G. (2010). Labeling live cells by copper-catalyzed alkyne–azide click chemistry. Bioconjug. Chem. *21*, 1912–1916.

Israels, R., Leermakers, F.A.M., Fleer, G.J., and Zhulina, E.B. (1994). Charged Polymeric Brushes: Structure and Scaling Relations. Macromolecules 27, 3249–3261.

Jung, Y., Riven, I., Feigelson, S.W., Kartvelishvily, E., Tohya, K., Miyasaka, M., Alon, R., and Haran, G. (2016). Three-dimensional localization of T-cell receptors in relation to microvilli using a combination of superresolution microscopies. Proc. Natl. Acad. Sci. USA *113*, E5916–E5924.

Kenworthy, A.K., Hristova, K., Needham, D., and McIntosh, T.J. (1995). Range and magnitude of the steric pressure between bilayers containing phospholipids with covalently attached poly(ethylene glycol). Biophys. J. 68, 1921–1936.

Kesavan, G., Sand, F.W., Greiner, T.U., Johansson, J.K., Kobberup, S., Wu, X., Brakebusch, C., and Semb, H. (2009). Cdc42-mediated tubulogenesis controls cell specification. Cell *139*, 791–801.

Kesimer, M., Ehre, C., Burns, K.A., Davis, C.W., Sheehan, J.K., and Pickles, R.J. (2013). Molecular organization of the mucins and glycocalyx underlying mucus transport over mucosal surfaces of the airways. Mucosal Immunol. 6, 379–392.

Koistinen, V., Kärnä, R., Koistinen, A., Arjonen, A., Tammi, M., and Rilla, K. (2015). Cell protrusions induced by hyaluronan synthase 3 (HAS3) resemble mesothelial microvilli and share cytoskeletal features of filopodia. Exp. Cell Res. 337, 179–191.

Kolata, G.B. (1975). Microvilli: a major difference between normal and cancer cells? Science 188, 819–820.

Kornberg, T.B., and Roy, S. (2014). Cytonemes as specialized signaling filopodia. Development *141*, 729–736.

Kovall, R.A., Gebelein, B., Sprinzak, D., and Kopan, R. (2017). The Canonical Notch Signaling Pathway: Structural and Biochemical Insights into Shape, Sugar, and Force. Dev. Cell *41*, 228–241.

Kozlovsky, Y., and Kozlov, M.M. (2003). Membrane fission: model for intermediate structures. Biophys. J. 85, 85–96.

Kramer, R.H., and Nicolson, G.L. (1979). Interactions of tumor cells with vascular endothelial cell monolayers: a model for metastatic invasion. Proc. Natl. Acad. Sci. USA *76*, 5704–5708.

Kufe, D.W. (2009). Mucins in cancer: function, prognosis and therapy. Nat. Rev. Cancer 9, 874–885.

Lange, K. (2011). Fundamental role of microvilli in the main functions of differentiated cells: Outline of an universal regulating and signaling system at the cell periphery. J. Cell. Physiol. 226, 896–927.

Lee, G.M., Johnstone, B., Jacobson, K., and Caterson, B. (1993). The dynamic structure of the pericellular matrix on living cells. J. Cell Biol. *123*, 1899–1907.

Lipowsky, R. (1995). Bending of Membranes by Anchored Polymers. EPL Europhys. Lett. 30, 197.

Liu, T.-L., Upadhyayula, S., Milkie, D.E., Singh, V., Wang, K., Swinburne, I.A., Mosaliganti, K.R., Collins, Z.M., Hiscock, T.W., Shea, J., et al. (2018). Observing the cell in its native state: Imaging subcellular dynamics in multicellular organisms. Science *360*, eaaq1392.

Lou, E., Fujisawa, S., Barlas, A., Romin, Y., Manova-Todorova, K., Moore, M.A.S., and Subramanian, S. (2012). Tunneling Nanotubes: A new paradigm for studying intercellular communication and therapeutics in cancer. Commun. Integr. Biol. *5*, 399–403.

Makabe, S., Naguro, T., and Stallone, T. (2006). Oocyte-follicle cell interactions during ovarian follicle development, as seen by high resolution scanning and transmission electron microscopy in humans. Microsc. Res. Tech. 69, 436–449.

Malaker, S.A., Pedram, K., Ferracane, M.J., Woods, E.C., Kramer, J., Dorigo, O., and Bertozzi, C. (2018). A Mucin-Specific Protease Enables Molecular and Functional Analysis of Human Cancer-Associated Mucins. ChemRxiv. Published online November 13. https://doi.org/10.26434/chemrxiv.7330676.v1.

Marshall, W.F. (2012). Organelle Size Control Systems: From Cell Geometry to Organelle-Directed Medicine. Bioessays *34*, 721–724.

McConnell, R.E., Higginbotham, J.N., Shifrin, D.A., Jr., Tabb, D.L., Coffey, R.J., and Tyska, M.J. (2009). The enterocyte microvillus is a vesicle-generating organelle. J. Cell Biol. *185*, 1285–1298.

McMaster, T.J., Berry, M., Corfield, A.P., and Miles, M.J. (1999). Atomic force microscopy of the submolecular architecture of hydrated ocular mucins. Biophys. J. 77, 533–541.

Menck, K., Bleckmann, A., Wachter, A., Hennies, B., Ries, L., Schulz, M., Balkenhol, M., Pukrop, T., Schatlo, B., Rost, U., et al. (2017). Characterisation of turnour-derived microvesicles in cancer patients' blood and correlation with clinical outcome. J. Extracell. Vesicles *6*, 1340745.

Milner, S.T. (1991). Polymer brushes. Science 251, 905-914.

Möckl, L., Pedram, K., Roy, A.R., Krishnan, V., Gustavsson, A.-K., Dorigo, O., Bertozzi, C., and Moerner, W.E. (2018). Quantitative Super-Resolution Microscopy of the Mammalian Glycocalyx. ChemRxiv. Published online November 27. https://doi.org/10.26434/chemrxiv.7381724.v1.

Mogilner, A., and Rubinstein, B. (2005). The physics of filopodial protrusion. Biophys. J. 89, 782–795.

Morlot, S., Galli, V., Klein, M., Chiaruttini, N., Manzi, J., Humbert, F., Dinis, L., Lenz, M., Cappello, G., and Roux, A. (2012). Membrane shape at the edge of the dynamin helix sets location and duration of the fission reaction. Cell *151*, 619–629.

Müller, S., Alving, K., Peter-Katalinic, J., Zachara, N., Gooley, A.A., and Hanisch, F.G. (1999). High density O-glycosylation on tandem repeat peptide from secretory MUC1 of T47D breast cancer cells. J. Biol. Chem. *274*, 18165–18172.

Muralidharan-Chari, V., Clancy, J.W., Sedgwick, A., and D'Souza-Schorey, C. (2010). Microvesicles: mediators of extracellular communication during cancer progression. J. Cell Sci. *123*, 1603–1611.

Ovesný, M., Křížek, P., Borkovec, J., Svindrych, Z., and Hagen, G.M. (2014). ThunderSTORM: a comprehensive ImageJ plug-in for PALM and STORM data analysis and super-resolution imaging. Bioinformatics *30*, 2389–2390.

Paluch, E.K., and Raz, E. (2013). The role and regulation of blebs in cell migration. Curr. Opin. Cell Biol. 25, 582–590.

Paszek, M.J., DuFort, C.C., Rubashkin, M.G., Davidson, M.W., Thorn, K.S., Liphardt, J.T., and Weaver, V.M. (2012). Scanning angle interference microscopy reveals cell dynamics at the nanoscale. Nat. Methods 9, 825–827.

Paszek, M.J., DuFort, C.C., Rossier, O., Bainer, R., Mouw, J.K., Godula, K., Hudak, J.E., Lakins, J.N., Wijekoon, A.C., Cassereau, L., et al. (2014). The cancer glycocalyx mechanically primes integrin-mediated growth and survival. Nature 511, 319-325.

Paturej, J., Sheiko, S.S., Panyukov, S., and Rubinstein, M. (2016). Molecular structure of bottlebrush polymers in melts. Sci. Adv. 2, e1601478.

Pelaseyed, T., Bergström, J.H., Gustafsson, J.K., Ermund, A., Birchenough, G.M.H., Schütte, A., van der Post, S., Svensson, F., Rodríguez-Piñeiro, A.M., Nyström, E.E.L., et al. (2014). The mucus and mucins of the goblet cells and enterocytes provide the first defense line of the gastrointestinal tract and interact with the immune system. Immunol. Rev. 260, 8-20.

Peskin, C.S., Odell, G.M., and Oster, G.F. (1993). Cellular motions and thermal fluctuations: the Brownian ratchet. Biophys. J. 65, 316-324.

Pilon, C., Levast, B., Meurens, F., Le Vern, Y., Kerboeuf, D., Salmon, H., Velge-Roussel, F., Lebranchu, Y., and Baron, C. (2009). CD40 engagement strongly induces CD25 expression on porcine dendritic cells and polarizes the T cell immune response toward Th1. Mol. Immunol. 46, 437-447.

Polefka, T.G., Garrick, R.A., Redwood, W.R., Swislocki, N.I., and Chinard, F.P. (1984). Solute-excluded volumes near the Novikoff cell surface. Am. J. Physiol. 247, C350-C356.

Raucher, D., and Sheetz, M.P. (1999). Characteristics of a membrane reservoir buffering membrane tension. Biophys. J. 77, 1992-2002.

Riemersma, M., Sandrock, J., Boltje, T.J., Büll, C., Heise, T., Ashikov, A., Adema, G.J., van Bokhoven, H., and Lefeber, D.J. (2015). Disease mutations in CMPsialic acid transporter SLC35A1 result in abnormal α-dystroglycan O-mannosylation, independent from sialic acid. Hum. Mol. Genet. 24, 2241-2246.

Satomaa, T., Heiskanen, A., Mikkola, M., Olsson, C., Blomqvist, M., Tiittanen, M., Jaatinen, T., Aitio, O., Olonen, A., Helin, J., et al. (2009). The N-glycome of human embryonic stem cells. BMC Cell Biol. 10, 42.

Sauvanet, C., Wayt, J., Pelaseyed, T., and Bretscher, A. (2015). Structure, regulation, and functional diversity of microvilli on the apical domain of epithelial cells. Annu. Rev. Cell Dev. Biol. 31, 593-621.

Saxer, R.A., Bent, S.J., Brower-Toland, B.D., Mi, Z., Robbins, P.D., Evans, C.H., and Nixon, A.J. (2001). Gene mediated insulin-like growth factor-I delivery to the synovium. J. Orthop. Res. 19, 759-767.

Schindelin, J., Arganda-Carreras, I., Frise, E., Kaynig, V., Longair, M., Pietzsch, T., Preibisch, S., Rueden, C., Saalfeld, S., Schmid, B., et al. (2012). Fiji: an open-source platform for biological-image analysis. Nat. Methods 9, 676–682. Schmick, M., and Bastiaens, P.I.H. (2014). The interdependence of membrane

shape and cellular signal processing. Cell 156, 1132-1138.

Schroeter, E.H., Kisslinger, J.A., and Kopan, R. (1998). Notch-1 signalling requires ligand-induced proteolytic release of intracellular domain. Nature 393, 382-386.

Seifert, U., Berndl, K., and Lipowsky, R. (1991). Shape transformations of vesicles: Phase diagram for spontaneous- curvature and bilayer-coupling models. Phys. Rev. A 44, 1182-1202.

Shurer, C.R., Colville, M.J., Gupta, V.K., Head, S.E., Kai, F., Lakins, J.N., and Paszek, M.J. (2017). Genetically Encoded Toolbox for Glycocalyx Engineering: Tunable Control of Cell Adhesion, Survival, and Cancer Cell Behaviors. ACS Biomater. Sci. Eng. 4, 388-399.

Snead, W.T., Hayden, C.C., Gadok, A.K., Zhao, C., Lafer, E.M., Rangamani, P., and Stachowiak, J.C. (2017). Membrane fission by protein crowding. Proc. Natl. Acad. Sci. USA 114, E3258-E3267.

Stachowiak, J.C., Schmid, E.M., Ryan, C.J., Ann, H.S., Sasaki, D.Y., Sherman, M.B., Geissler, P.L., Fletcher, D.A., and Hayden, C.C. (2012). Membrane bending by protein-protein crowding. Nat. Cell Biol. 14, 944–949.

Stolfa, G., Mondal, N., Zhu, Y., Yu, X., Buffone, A., Jr., and Neelamegham, S. (2016). Using CRISPR-Cas9 to quantify the contributions of O-glycans, N-glycans and Glycosphingolipids to human leukocyte-endothelium adhesion. Sci. Rep. 6, 30392.

Tillberg, P.W., Chen, F., Piatkevich, K.D., Zhao, Y., Yu, C.C., English, B.P., Gao, L., Martorell, A., Suk, H.J., Yoshida, F., et al. (2016). Protein-retention expansion microscopy of cells and tissues labeled using standard fluorescent proteins and antibodies. Nat. Biotechnol. 34, 987-992.

Tricarico, C., Clancy, J., and D'Souza-Schorey, C. (2017). Biology and biogenesis of shed microvesicles. Small GTPases 8, 220-232.

Tsafrir, I., Sagi, D., Arzi, T., Guedeau-Boudeville, M.-A., Frette, V., Kandel, D., and Stavans, J. (2001). Pearling instabilities of membrane tubes with anchored polymers. Phys. Rev. Lett. 86, 1138-1141.

Turley, E.A., Wood, D.K., and McCarthy, J.B. (2016). Carcinoma Cell Hyaluronan as a "Portable" Cancerized Prometastatic Microenvironment. Cancer Res. 76, 2507-2512.

van den Pol, A.N., and Kim, W.T. (1993). NILE/L1 and NCAM-polysialic acid expression on growing axons of isolated neurons. J. Comp. Neurol. 332,

Walter, D.M., Venancio, O.S., Buza, E.L., Tobias, J.W., Deshpande, C., Gudiel, A.A., Kim-Kiselak, C., Cicchini, M., Yates, T.J., and Feldser, D.M. (2017). Systematic In Vivo Inactivation of Chromatin-Regulating Enzymes Identifies Setd2 as a Potent Tumor Suppressor in Lung Adenocarcinoma. Cancer Res. 77, 1719-1729.

Wang, Y., Ju, T., Ding, X., Xia, B., Wang, W., Xia, L., He, M., and Cummings, R.D. (2010). Cosmc is an essential chaperone for correct protein O-glycosylation, Proc. Natl. Acad. Sci. USA 107, 9228-9233.

Weichsel, J., and Geissler, P.L. (2016). The More the Tubular: Dynamic Bundling of Actin Filaments for Membrane Tube Formation. PLoS Comput. Biol. 12. e1004982.

Weisshuhn, P.C., Sheppard, D., Taylor, P., Whiteman, P., Lea, S.M., Handford, P.A., and Redfield, C. (2016). Non-Linear and Flexible Regions of the Human Notch1 Extracellular Domain Revealed by High-Resolution Structural Studies. Structure 24, 555-566.

Ying, H., Kimmelman, A.C., Lyssiotis, C.A., Hua, S., Chu, G.C., Fletcher-Sananikone, E., Locasale, J.W., Son, J., Zhang, H., Coloff, J.L., et al. (2012). Oncogenic Kras maintains pancreatic tumors through regulation of anabolic glucose metabolism. Cell 149, 656-670.

Yuan, H., Tank, M., Alsofyani, A., Shah, N., Talati, N., LoBello, J.C., Kim, J.R., Oonuki, Y., de la Motte, C.A., and Cowman, M.K. (2013). Molecular mass dependence of hyaluronan detection by sandwich ELISA-like assay and membrane blotting using biotinylated hyaluronan binding protein. Glycobiology 23, 1270-1280

Zeng, Y., Ramya, T.N.C., Dirksen, A., Dawson, P.E., and Paulson, J.C. (2009). High-efficiency labeling of sialylated glycoproteins on living cells. Nat. Methods 6, 207-209.

Zhang, H., Miller, R.H., and Rutishauser, U. (1992). Polysialic acid is required for optimal growth of axons on a neuronal substrate. J. Neurosci. 12, 3107-3114

Zhulina, E.B., and Borisov, O.V. (1996). Polyelectrolytes Grafted to Curved Surfaces. Macromolecules 29, 2618-2626.

Zhulina, E.B., Birshtein, T.M., and Borisov, O.V. (2006). Curved polymer and polyelectrolyte brushes beyond the Daoud-Cotton model. Eur Phys J E Soft Matter 20, 243-256.

STAR***METHODS**

KEY RESOURCES TABLE

REAGENT or RESOURCE	SOURCE	IDENTIFIER
Antibodies		
FITC Mouse Anti-Human MUC1 (CD227)	BD Biosciences	Cat# 559774; RRID: AB_397318
Purified Mouse Anti-Human MUC1 (CD227)	BD Biosciences	Cat# 555925; RRID: AB_396226
Human Podocalyxin Mab (Clone 222328) antibody	R and D Systems	Cat# MAB1658; RRID: AB_2165984
Actin (C-11) antibody	Santa Cruz Biotechnology	Cat# sc-1615; RRID: AB_630835
GFP (4B10) Mouse mAb antibody	Cell Signaling Technology	Cat# 2955; RRID: AB_1196614
SxHis antibody	BD Biosciences	Cat# 552565; RRID: AB_394432
Goat Anti-Mouse IgG-HRP Polyclonal antibody	Santa Cruz Biotechnology	Cat# sc-2005; RRID: AB_631736
Mouse Anti-Goat IgG-HRP antibody	Santa Cruz Biotechnology	Cat# sc-2354; RRID: AB_628490
Bacterial and Virus Strains		
Stbl3 E. coli	ThermoFisher Scientific	Cat# C7373
(L1-Blue E. coli	Agilent / Stratagene	Cat# 200236
Chemicals, Peptides, and Recombinant Proteins		
Hyaluronic Acid Binding Protein (HABP), Bovine Nasal Cartilage, Biotinylated	Millipore Sigma	Cat# 385911
Hyaluronic Acid Binding Protein (HABP), Bovine Nasal Cartilage	Millipore Sigma	Cat# 385910
_atrunculin A (LatA)	Cayman Chemical	Cat# 10010630
1,2-dioleoyl-sn-glycero-3-phosphocholine (DOPC)	Avanti Polar Lipids	Cat# 850375P
,2-dioleoyl-sn-glycero-3-[(N-(5-amino-1-carboxypentyl) minodiacetic acid)succinyl] (nickel salt)	Avanti Polar Lipids	Cat# 790404P
B-BODIPY FL C5-HPC (BODIPY PC)	Thermo Fisher Scientific	Cat# D3803
Recombinant Human Podocalyxin Protein, CF	R and D Systems	Cat# 1658-PD
GFP Binding Protein (Nanobody)	Chromotek	Cat# gt-250
Alexa Fluor 647 NHS Ester (Succinimidyl Ester)	ThermoFisher Scientific	Cat# A37573
Alexa Fluor 568 NHS Ester (Succinimidyl Ester)	ThermoFisher Scientific	Cat# A20003
Alexa Fluor 488 NHS Ester (Succinimidyl Ester)	ThermoFisher Scientific	Cat# A20000
6% Parafomaldehyde (formaldehyde) aqueous solution	Fisher Scientific	Cat# 50-980-487
0% Glutaraldehyde aqueous solution	Fisher Scientific	Cat# 50-262-13
1% Osmic acid in aqueous solution	VWR	Cat# 100504-822
FreeStyle 293 Expression Medium	ThermoFisher Scientific	Cat# 12338018
DMEM/F12	ThermoFisher Scientific	Cat# 11320033
Horse serum, New Zealand origin	ThermoFisher Scientific	Cat# 16050122
Recombinant Murine EGF	Peprotech	Cat# 315-09
nsulin solution from bovine pancreas	Millipore Sigma	Cat# I0516
Hydrocortisone	Millipore Sigma	Cat# H0888
Cholera Toxin from Vibrio cholerae	Millipore Sigma	Cat# C8052
Penicillin-Streptomycin	ThermoFisher Scientific	Cat# 15140122
DMEM, high glucose	ThermoFisher Scientific	Cat# 11965118
Fetal Bovine Serum, qualified, USDA-approved regions	ThermoFisher Scientific	Cat# 10437028
RPMI 1640 Medium	ThermoFisher Scientific	Cat# 11875093
FreeStyle MAX Reagent	ThermoFisher Scientific	Cat# 16447100
G418, Geneticin	ThermoFisher Scientific	Cat# 10131035

Continued		
REAGENT or RESOURCE	SOURCE	IDENTIFIER
Puromycin	Millipore Sigma	Cat# P8833
Hygromycin B	Millipore Sigma	Cat# 10843555001
Blasticidin	InvivoGen	Cat# ant-bl-1
Doxycycline Hyclate	Santa Cruz Biotechnology	Cat# sc-204734
Doxycycline Hyclate	Applichem	Cat# A2951,0025
Clarity Western ECL Substrate	Bio-Rad	Cat# 1705061
Normal Goat Serum	Vector Laboratories	Cat# S-1000
StcE Mucinase	Malaker et al., 2018	N/A
Peanut agglutinin (PNA) antibody, biotinylated	Vector Laboratories	Cat# B-1075
CF-568 Dye PNA Lectin (Arachis hypogaea)	Biotium	Cat# 29061
CF-640R Dye PNA Lectin (Arachis hypogaea)	Biotium	Cat# 29063
CF-633 Dye Wheat Germ Agglutinin (WGA)	Biotium	Cat# 29024
Biotinylated Vicia Villosa Lectin (VVL, VVA)	Vector Laboratories	Cat# B-1235
ExtrAvidin-Peroxidase antibody	Sigma-Aldrich	Cat# e2886
Streptavidin-HRP	R and D Systems	Cat# DY998
NeutrAvidin Protein, DyLight 650	Thermo Fisher Scientific	Cat# 84607
Ac₄GalNAz	Thermo Fisher Scientific	Cat# 88905
Alexa Fluor 647 Alkyne, Triethylammonium Salt	Thermo Fisher Scientific	Cat# A10278
ВТТАА	Click Chemistry Tools	Cat# 1236
AlexaFluor-647-hydroxylamine	Thermo Fisher Scientific	Cat# A30632
Apo-Transferrin human	Millipore Sigma	Cat# T2036
GFP booster Atto 647N (GFP nanobody)	Chromotek	Cat# gba647n-100
HisPur Ni-NTA Resin	Thermo Fisher Scientific	Cat# 88221
SYPRO Ruby Protein Gel Stain	Thermo Fisher Scientific	Cat# S12000
Alexa Fluor 568 Phalloidin	Thermo Fisher Scientific	Cat# A12380
N-azidoacetylmannosamine-tetraacylated (Ac4ManNAz)	Click Chemistry Tools	Cat# 1084-5
AFDye 647 DBCO	Click Chemistry Tools	Cat# 1302-1
Acryloyl-X, SE, 6-((acryloyl)amino)hexanoic Acid, Succinimidyl Ester	Invitrogen	Cat# A20770
sodium acrylate	Millipore Sigma	Cat# 45-408220
10% acrylamide solution	Biorad	Cat# 1610140
2% bis-acrylamide solution	Biorad	Cat# 1610142
Ammonium persulfate	Millipore Sigma	Cat# A3678
Tetramethylethylenediamine	Millipore Sigma	Cat# T9281
ow glucose (1.0 g/L) DMEM media	Hyclone	Cat# SH30021.01
HEPES	Corning	Cat# 25-060-CI
Fetal bovine serum (for primary cells)	VWR	Cat# 97068-085
Penicillin/streptomycin (for primary cells)	Corning	Cat# 30-002-CI
Collagenase	Worthington Biochemical	Cat# LS004177
DNase I	Roche	Cat# 10104159001
Ham's F12 media	Corning	Cat# 10-080-CV
Hyaluronidase	Millipore Sigma	Cat# 389561
ECL substrate (for HA blot)	Amresco	Cat# 1B1581-kit-100ml
Cysteamine	Millipore Sigma	Cat# 30070
Catalase from bovine liver	Millipore Sigma	Cat# C100
Glucose oxidase	Millipore Sigma	Cat# G2133-50KU
Glucose	BD Difco	Cat# 215530
	DD D1100	J 10000

IDENTIFIER
Cat# 3438-100-1
Cat# 15567-027
Cat# DY3614
Cat# VVCA-1003
Cat# K1231
Cat# CRL-10317; RRID: CVCL_0598
Cat# CRL-3216; RRID: CVCL_0063
Cat# HTB-133; RRID: CVCL_0553
Cat# CRL-1500; RRID: CVCL_0588
Cat# CCL-2; RRID: CVCL_0030
Cat# R79007
N/A
N/A
N/A

Continued		
REAGENT or RESOURCE	SOURCE	IDENTIFIER
Human COSMC guide RNA: 5'-GAGTCTTTGGGCTG CAGTAA-3'	Stolfa et al., 2016	N/A
Human SLC35A1 guide RNA: 5'-TTCTGTGATACACAC GGCTG-3'	This Paper	N/A
Notch1 FWD primer: 5'- GGCAAGATCTCTAGAGGC FTGAGATGCTCCCAGCCA -3'	This Paper	N/A
Notch1 REV primer: 5'- GGCACCTGAGGCGTGGCA CAGTAGCCCGTTGAATTTG -3'	This Paper	N/A
Recombinant DNA		
pLV rtTA-NeoR plasmid	Paszek et al., 2014	N/A
Hyperactive Transposase plasmid	Shurer et al., 2017	N/A
pPB tetOn PuroR plasmid	Shurer et al., 2017	N/A
/luc1-42TR ΔCT pPB tetOn PuroR plasmid	Shurer et al., 2017	N/A
Muc1-42TR TM21 pPB tetOn PuroR plasmid	Shurer et al., 2017	N/A
Podxl ΔCT pPB tetOn PuroR plasmid	Shurer et al., 2017	N/A
Muc1 GFP ΔCT pPB tetOn PuroR	Shurer et al., 2017	N/A
Rational GFP ΔCT (9-80) pPB tetOn PuroR plasmid	This Paper	N/A
Muc1 0TR GFP ΔCT pPB tetOn PuroR plasmid	This Paper	N/A
Muc1 10TR GFP ΔCT pPB tetOn PuroR plasmid	This Paper	N/A
Muc1 42TR GFP ΔCT pPB tetOn PuroR plasmid	This Paper	N/A
lotch1 GFP ΔCT pPB tetOn PuroR plasmid	This Paper	N/A
LV tetOn HygroR HAS3 plasmid	This Paper	N/A
SUMO Muc1-42TR GPF ΔCT pPB tetOn PuroR plasmid	This Paper	N/A
oLV HygroR tetOn plasmid	Paszek et al., 2012	N/A
Human Hyaluronan Synthase 3/HAS3 (NP_005320) plasmid	R and D Systems	Cat# RDC0920
noxGFP plasmid	Costantini et al., 2015	Cat# 68070, Addgene #68070
66 Muc1-42TR 10xHis pPB tetOn PuroR plasmid	This Paper	N/A
SxHis SUMO pcDNA3.1, custom gene synthesis plasmid	General Biosystems	N/A
Muc1 42TR GFP ΔCT pcDNA3.1, custom gene synthesis	General Biosystems	N/A
entiCRISPR v2 Blast plasmid	Mohan Babu	Cat# 83480, Addgene #83480
entiCRISPR v2 GFP plasmid	Walter et al., 2017	Cat# 82416, Addgene #82416
COSMC lentiCRISPR v2 Blast plasmid	This Paper	N/A
SLC35A1 lentiCRISPR v2 GFP plasmid	This Paper	N/A
oCS2 Notch1 Full Length-6MT plasmid	Schroeter et al., 1998	Cat# 41728, Addgene #41728
Software and Algorithms		
Nanoparticle Tracking Analysis software	Malvern Panalytical	https://www.malvernpanalytical.com/ en/products/technology/nanoparticle- tracking-analysis
Prism 8.0	GraphPad	https://www.graphpad.com/scientific-software/prism/
BoxPlotR	Online	http://shiny.chemgrid.org/boxplotr/
FlowJo v10	FlowJo, LLC	https://www.flowjo.com/solutions/ flowjo/downloads
BD FACSDiva Software 8.0.1	BD Biosciences	N/A
CFlow Plus Analysis v1.0.227.4	BD Biosciences	http://www.bdbiosciences.com/us/ instruments/research/cell-analyzers/ bd-accuri/m/1294932/features/software
mage Lab v5.2.1	Bio-Rad	http://www.bio-rad.com/en-us/product/ image-lab-software?ID=KRE6P5E8Z
		(Continued on next no

Continued		
REAGENT or RESOURCE	SOURCE	IDENTIFIER
Fiji	NIH	https://fiji.sc/
Matlab 2015b	MathWorks	https://www.mathworks.com/help/matlab/release-notes-R2015b.html
Adobe Photoshop CC	Adobe	https://www.adobe.com/products/ photoshop.html
Adobe Illustrator CC	Adobe	https://www.adobe.com/products/ illustrator.html

CONTACT FOR REAGENT AND RESOURCE SHARING

Further information and requests for resources and reagents should be directed to and will be fulfilled by the Lead Contact, Matthew Paszek (mjp31@cornell.edu). All plasmids used in this work will be made available to the community through the Addgene repository or directly from the Lead Contact.

EXPERIMENTAL MODEL AND SUBJECT DETAILS

Cell Lines

Parental Cell Lines

MCF10A cells were cultured in DMEM/F12 media supplemented with 5% horse serum, 20 ng/mL EGF, 10 μ g/ml insulin, 500 ng/mL hydrocortisone, 100 ng/mL cholera toxin and penicillin/streptomycin. HEK293T and HeLa cells were cultured in DMEM high glucose media supplemented with 10% fetal bovine serum and penicillin/streptomycin. T47D cells were cultured in RPMI media supplemented with 10% fetal bovine serum, 10 μ g/ml insulin, and penicillin/streptomycin. FreeStyle 293-F cells were maintained in Freestyle 293 Expression Medium in spinner flasks at 37°C, 8% CO₂, 120 RPM, and 80% RH according to manufacturer's protocol.

Generated Cell Lines

Stable MCF10A, primary equine synoviocyte, and 293-F cells expressing the rtTA-M2 tetracycline transactivator were prepared by lentiviral transduction using the pLV rtTA-NeoR plasmid as previously described (Paszek et al., 2012). Cells were further modified with tetracycline-responsive promoter plasmids. Stable cells expressing hyaluronan synthase 3 (HAS3) were prepared by lentiviral transduction using the pLV HygroR tetOn HAS3 plasmid. For preparation of the mucin-expressing cell lines and Notch1- expressing cell line (EGF-repeats GFP Δ CT), plasmids with ITR-flanked expression cassettes (i.e. pPB tetOn PuroR plasmids) were co-transfected with the PiggyBac hyperactive transposase using Nucleofection Kit V (Lonza) or FreeStyle Max Reagent (Thermo Fisher) according to manufacturer's protocols. For CRISPR knockouts, cell lines expressing Muc1-42TR Δ CT were further modified by lentiviral transduction using either SLC35A1 lentiCRISPR v2 GFP or COSMC lentiCRISPR v2 Blast plasmids. Selection of stable cell lines was performed with 750 μ g/mL G418, 1 μ g/mL puromycin, 200 μ g/mL hygromycin, or 15 μ g/ml Blasticidin.

Primary Synoviocyte Isolation and Culture

Primary equine synoviocytes were obtained from the shoulder, stifle, carpal, tarsal, and fetlock joints of a male thoroughbred yearling horse (*Equus caballus*). To isolate the fibroblast-like type B synovial cells (synoviocytes), synovial membrane tissues were digested with 0.15% collagenase (Worthington Biochemical, Lakewood, NJ) supplemented with 0.015% DNase I (Roche, Indianapolis, IN) for 3 h at 37°C in Ham's F12 media, followed by filtration and centrifugation at 250x *g* for 10 min as previously described (Saxer et al., 2001). Equine synoviocytes were cultured in low glucose (1.0 g/L) DMEM media supplemented with 40 mM HEPES, 4 mM L-Glutamine, 110 mg/L sodium pyruvate, 10% fetal bovine serum and penicillin/streptomycin. Subculture of the synoviocytes was performed every 3–4 days. All adherent cells were maintained at 37°C, 5% CO₂, and 90% RH.

Equine Synovial Tissue Resection

Synovial tissues were harvested from the middle carpal joint of two adult thoroughbred horses. The freshly resected tissues were either incubated for 30 min in Ham's F12 media with or without 1 U/mL Hyaluronidase (Sigma) and fixed or immediately fixed for 24 h with 4% paraformaldehyde and 1% glutaraldehyde in PBS. Tissues were then either processed for SEM or reduced with 0.1 mg/mL NaBH₄ for 20 min on ice and further processed for confocal imaging.

METHOD DETAILS

Cloning and Constructs

cDNAs for cytoplasmic-tail-deleted human Muc1 with 42 tandem repeats (Muc1-42TR Δ CT), Muc1-42TR polymer domain fusion with the TM21 synthetic membrane domain (Muc1-42TR TM21), cytoplasmic-tail-deleted human Podocalyxin (S/T-Rich Δ CT)

were generated and cloned into the tetracycline-inducible PiggyBac expression vector (pPB tetOn PuroR) or mammalian expression vector pcDNA3.1 as previously described (Paszek et al., 2014; Shurer et al., 2017). To make lentiviral vector pLV HygroR tetOn HAS3, the cDNA for human HAS3 (accession NP_005320) was obtained from R&D Systems and amplified via PCR with the forward primer, 5'-GGCACCTCGAGGATGCCGGTGCAGCTGACGACA-3', and reverse primer, 5'-GGCAGAATTCTTACACCTCAGCAAAAGCC AAGCT - 3'. The PCR product was cloned into pJET1.2 (ThermoFisher) according to manufacturer's protocol, and subcloned into the Absl and EcoRI sites of pLV HygroR tetOn (Paszek et al., 2012). For generation of Muc1 GFP ΔCT pPB tetOn PuroR with varying number of tandem repeats, the cDNA for mOxGFP (Addgene #68070; heretofore mOxGFP is referred to as GFP) was amplified with primers: 5'- GGCAGCTCAGCTATGGTGTCCAAGGGCGAGGAGCTGT-3' (forward) and 5'- GGCAGCTGAGCCCTTATACAG CTCGTCCATGCCGTGAGT-3' (reverse). The PCR product was cloned into pJET1.2 and subcloned non-directionally into the Blpl site of Muc1-42TR Δ CT pPB tetOn PuroR. For constructs with 10 and 42 native tandem repeats (PDTRPAPGSTAPPAHGVTSA), synthetic cDNAs for the desired repeat units were generated through custom gene synthesis (General Biosystems) and cloned in place of the tandem repeats in Muc1 GFP ΔCT pPB tetOn PuroR using the BamHl and Bsu36l restriction sites. Muc1 tandem repeats were deleted through Q5 site directed mutagenesis with 5'-TGGAGGAGCCTCAGGCATACTTTATTG-3' (forward) and 5'-CCACCGCC GACCGAGGTGACATCCTG-3' (reverse) primers to generate Muc1 0TR GFP ΔCT pPB tetOn PuroR. To add a SumoStar tag to the Muc1-42TR GFP ΔCT N terminus, a cDNA encoding the IgG kappa leader sequence, SumoStar tag, and Muc1 N terminus was generated through custom gene synthesis (General Biosystems) and inserted in place of the Muc1 N terminus in Muc1 GFP ΔCT pPB tetOn PuroR using the BamHI and BsrGI restriction sites. For construction of both COSMC and SLC35A1 vectors, we used the pLentiCRISPRv2 system. The target sequence for human COSMC (5'-GAGTCTTTGGGCTGCAGTAA-3') was cloned into the pLentiCRISPRv2 Blast backbone (Addgene #83480). The target sequence for human SLC35A1 (5'-TTCTGTGATACACAC GGCTG-3') was cloned into the pLentiCRISPRv2 GFP backbone (Addgene #82416), both after BsmBI digestion.

For generation of the Notch1 GFP ΔCT pPB tetOn PuroR plasmid (EGF-repeats GFP ΔCT), the cDNA for Notch1 (Addgene #41728) was amplified with primers: 5'- GGCAAGATCTCTAGAGGCTTGAGATGCTCCCAGCCA -3' (forward) and 5'- GGCACCTGAGG CGTGGCACAGTAGCCCGTTGAATTTG -3' (reverse). The PCR product was cloned into the Bglll and Bsu36l sites of the Muc1 42TR ΔCT pPB tetOn PuroR plasmid.

For recombinant production of the mucin polymer domain, 42 tandem repeats from Muc1 were fused to an N-terminal S6 tag (GDSLSWLLRLLN) and C-terminal 10x-histidine purification tag to make Muc1-42TR 10X His. To insert the S6 tag, Q5 site directed mutagenesis was performed using 5'-GTTGCGACTGCTTAACGGACAGATCTCGATGGTGAGC-3' (forward) and 5'-AGCCAGCT CAGGGAATCCCCAGCATTCTTCTCAGTAGAG-3' (reverse) on a pcDNA3.1 plasmid containing the Muc1 N terminus from Muc1-42TR ACT pPB tetOn PuroR between BamHI and BgIII sites. The S6 tag was subsequently cut at these sites and replaced in the Muc1-42TR ΔCT N terminus in Muc1-42TR ΔCT pPB tetOn PuroR. The 10x-histidine tag was added by annealing the oligos, 5'-TCAGGCCACCACCACCATCACCATCACCACTATGGG-3' and 3'-CCGGTGGTGGTGGTAGTGGTAGTGGTGGTAGTAGTGGTAA TCCCTTAA-5' and inserting in place of the Muc1-42TR ΔCT C terminus in Muc1-42TR ΔCT pPB tetOn PuroR using the Bsu36I and EcoRI restriction sites.

Immuno- and Lectin Blot Analysis

Cells were plated at 20,000 cells/cm² and induced with 0.2 μg/mL doxycycline (Santa Cruz) for 24 h before lysis with Tris-Triton lysis buffer (Abcam). Lysates were separated on Nupage 4%-12% Bis-Tris or 3%-8% Tris-Acetate gels (Thermo Fisher) and transferred to PVDF membranes. Primary antibodies were diluted 1:1000 and lectins were diluted to 1 μg/mL in 3% BSA TBST and incubated 4 h at room temperature or overnight at 4°C. Secondary antibodies or ExtrAvidin were diluted 1:2000 in 3% BSA TBST and incubated for 2 h at room temperature. Blots were developed in Clarity ECL (BioRad) substrate, imaged on a ChemiDoc (BioRad) documentation system, and quantified in ImageJ Fiji (Schindelin et al., 2012).

Flow Cytometric Analysis

Cells were plated at 20,000 cells/cm² and grown for 24 h. Cells were then induced with 0.2 μg/mL doxycycline (Santa Cruz) for 24 h. For sialic acid labeling by ManNAz, separate cultures were plated in parallel with cells treated for 24 h with both 0.2 μg/mL doxycycline (Santa Cruz) and 25 μ M Ac₄ManNAz (Click Chemistry Tools). Ac₄ManNAz treated cells were labeled with 50 μ M AF647 DBCO in 1% FBS PBS for 20 min at room temperature. Adherent cells were non-enzymatically detached by incubating with 1 mM EGTA in PBS at 37°C for 20 min and added to the population of floating cells, if present. Affinity reagents: anti-Muc1, GFP nanobody, 650 Neutravidin were diluted 1:200 in 0.5% BSA PBS; 647 PNA and biotin VVA were diluted to 1 μg/mL in 0.5% BSA PBS and incubated with cells at 4°C for 30 min for each stain. A BD Accuri C6 flow cytometer was used for analysis.

Confocal Microscopy for Cells and Tissues

Cells were plated at 5,000 cells/cm² and subsequently induced with 0.2 μg/mL of doxycycline (Santa Cruz) for 24 h before being fixed with 4% paraformaldehyde. Antibodies and HABP were diluted 1:200 in 5% normal goat serum (Vector Laboratories) in PBS and incubated overnight at 4°C. For fluorescent HABP, HABP (Millipore Sigma) was labeled with Alexa Fluor 568 NHS Ester (Thermo Fisher Scientific) per the manufacturer's protocol. Lectins were diluted to 1 μg/mL in 5% normal goat serum in PBS and incubated for 2 h at room temperature. For hyaluronic acid staining of cells and tissues, HABP was diluted to 0.125 μg/ml in 0.5% normal goat serum in PBS and incubated on samples for 24 h. Cell samples were imaged on a Zeiss LSM inverted 880 confocal microscope using a $40 \times$ water immersion objective (NA 1.1). In addition to HABP, NaBH₄-treated tissues were stained with 1 μ g/mL Hoechst for 10 min and imaged on a Zeiss 880 upright confocal microscope with a $40 \times$ water dipping lens. Unstained tissue collagen was visualized with second harmonic generation using non-descan detectors.

Scanning Electron Microscopy

All samples were fixed for 24 h with 4% paraformaldehyde and 1% glutaraldehyde in PBS, post-fixed for 45 min with 1% osmium tetraoxide in dH $_2$ O, washed and subsequently dehydrated stepwise in ethanol of 25%, 50%, 70%, 95%, 100%, 100% before drying in a critical point dryer (CPD 030, Bal-Tec). Samples were coated with gold-palladium in a Desk V sputter system (Denton Vacuum) and imaged on a field emission scanning electron microscope (Mira3 FE-SEM, Tescan or FE-SEM LEO 1550, Carl Zeiss). For actin depolymerization studies, cells were treated for 60 min with 10 μ M LatA (Cayman Chemical) before fixation, where indicated.

Mucin Digestion and Super-Resolution Imaging Sample prep and azido sugars incorporation

MCF10A Muc1-42TR Δ CT cells were cultured in phenol red free 1:1 DMEM:F12 supplemented as described previously. For imaging, cells were seeded at a density of 10,000 cells/well on Lab-Tek II Chambered Coverglass (Thermo Fisher Scientific) coated with 0.01% poly-Lysine (Sigma). Media was supplemented with Ac₄GalNAz (Thermo Fisher Scientific) 2 h post-seeding at a concentration of 50 μ M. For induction of Muc1-42TR Δ CT expression, doxycycline (Applichem) was added to Lab-Tek wells 16 h post-seeding at 200 ng/mL. Enzymatic de-mucination was performed 24 h post-doxycycline induction with 50 nM StcE in complete media for 2 h at 37°C immediately before labeling and imaging (Malaker et al., 2018; Möckl et al., 2018).

Cu-click Labeling of GalNAc

Cells were moved to 4° C and washed three times with cold DPBS with Ca^{2+} and Mg^{2+} . Immediately after washing, Cu-click conjugation with AlexaFluor-647-alkyne (Thermo Fisher Scientific) was performed. The cells were incubated with 50 μ M CuSO₄ (Sigma), 250 μ M BTTAA (Click Chemistry Tools), 1 mM aminoguanidine (Sigma), 2.5 mM sodium ascorbate (Sigma), and 25 μ M AlexaFluor-647-alkyne (Thermo Fisher Scientific) in DPBS for 5 min at 4° C as reported previously (Hong et al., 2010). Cells were washed five times with cold DPBS and fixed with 4° C paraformaldehyde (Thermo Fisher Scientific) and 0.2% glutaraldehyde (Sigma) in DPBS for 30 min at room temperature.

Periodate-Mediated Labeling of Sialic Acids

Sialic acids were labeled as described previously (Zeng et al., 2009). Cells were moved to 4° C, then washed three times with cold DPBS with Ca²⁺ and Mg²⁺ followed by a 5-minute incubation with 1 mM sodium periodate (Sigma) in DPBS. The periodate was quenched by 1 mM glycerol in cold DPBS and washed three times with cold DPBS. Samples were stained with 25 μ M AlexaFluor-647-hydroxylamine (Thermo Fisher Scientific) in the presence of 10 mM aniline in sterile filtered DPBS + 5% FBS pH 6.7 for 30 min at 4°C in the dark with gentle agitation. Cells were washed five times with cold DPBS and fixed with 4% paraformal-dehyde (Thermo Fisher Scientific) and 0.2% glutaraldehyde (Sigma) in DPBS for 30 min at room temperature.

Optical Setup

The core of the setup was an inverted microscope (IX71, Olympus, Tokyo, Japan). The laser used for illumination (120 mW 647 nm, CW, Coherent, Santa Clara, CA) was spectrally filtered (ff01-631/36-25 excitation filter, Semrock, Rochester, NY) and circularly polarized (LPVISB050-MP2 polarizers, Thorlabs, Newton, NJ, WPQ05M-633 quarter-wave plate, Thorlabs). The beam was expanded and collimated using Keplerian telescopes. Shutters were used to toggle the lasers (VS14S2T1 with VMM-D3 three-channel driver, Vincent Associates Uniblitz, Rochester, NY). The laser was introduced into the back port of the microscope via a Köhler lens. The sample was mounted onto an XYZ stage (Plnano XYZ Piezo Stage and High Precision XY Microscope Stage, Physik Instrument, Karlsruhe, Germany). Emitted light was detected by a high NA detection objective (UPLSAPO100XO, x100, NA 1.4, Olympus) and spectrally filtered (Di01-R405/488/561/635 dichroic, Semrock, ZET647NF notch filter, Chroma, Bellows Falls, VT, ET700/75m.

Image Acquisition and Analysis for SR Microscopy

For single-molecule localization microscopy, a reducing, oxygen scavenging buffer (Halpern et al., 2015) consisting of 20 mM cyste-amine, 2 μ L/mL catalase, 560 μ g/mL glucose oxidase (all Sigma-Aldrich), 10% (w/v) glucose (BD Difco, Franklin Lakes, NJ), and 100 mM Tris-HCl (Life Technologies) was added. Image acquisition was started after a short delay needed to convert the majority of the fluorophores into a dark state at a laser intensity of 5 kW/cm². The exposure time was 50 ms and the calibrated EM gain was 186. SR images were reconstructed from approximately 40,000 frames using the ImageJ plugin Thunderstorm (Ovesný et al., 2014). The frames were filtered with a B-spline filter of order 3 and scale 2.0. Single-molecule signals were detected with 8-neighborhood connectivity and a threshold of three times the standard deviation of the first wavelet level. Detected local maxima were fitted with a 2D-Gaussian using least squares. Post-processing involved drift correction by cross-correlation, followed by filtering (settings: sigma of the fitted Gaussian < 200 nm; uncertainty of localization < 20 nm). Images were reconstructed as 2D histograms with bin size = 32 nm.

Giant Unilamellar Vesicles

Giant Unilamellar Vesicles (GUVs) were prepared by electroformation as described previously (Angelova and Dimitrov, 1986). Briefly, lipids and dye dissolved in chloroform were spread on glass slides coated with ITO (Indium-Tin-Oxide). The slides were placed under vacuum for 2 h to remove all traces of organic solvents. The lipid films were hydrated and swelled in 120 mM sucrose at 55°C. GUVs

were electroformed by the application of an oscillating potential of 1.4 V (peak-to-peak) and 12 Hz for 3 h (Busch et al., 2015). GUVs compositions were prepared with DOPC and increasing molar fractions of DOGS-Ni-NTA lipid (5, 10, 15, and 20 mol%). Bodipy-PC was used to label the lipids at a dye/lipid ratio of 1/2500. Recombinant His-tagged Podocalyxin was conjugated with Alexa Fluor 568 NHS Ester (Thermo Fisher Scientific), and the degree of labelling quantified according to the manufacturer's protocol. GUVs were diluted in 20 mM HEPES, 50 mM NaCl, pH = 7.4 (120 mOsm) and then mixed with labeled Podocalyxin (~2 μM) for at least 20 min before imaging (GUVs/proteins = 1/1 by volume). GUVs were imaged on a Nikon C2plus confocal microscope using a 60x water immersion objective (NA 1.2). Lipids (Bodipy-PC) and protein (Alexa Fluor 568) were imaged through excitation at wavelength λ =488 and 561 nm, respectively.

Endocytosis Assay

Human apo-Transferrin (Sigma) was diluted to 1 mg/mL in PBS and labeled with Alexa Fluor 488 NHS Ester (Thermo Fisher Scientific) per manufacturer's protocol. Cells were prepared by plating and inducing wild-type (Control) and Muc1-42TR ΔCT-expressing MCF10A cells with 0.2 μg/mL of doxycycline (Santa Cruz) for 18 h. The 488-labled transferrin was diluted 1:1000 into fresh cell culture media with doxycycline (Santa Cruz) and incubated at 37°C, 5% CO₂ with cells for 30 min or 60 min. Cells were then detached with 0.05% trypsin EDTA (Thermo Fisher Scientific). Cells were washed with ice cold 0.5% BSA in PBS. Fluorescent signal was measured using a BD Accuri C6 flow cytometer. Confocal images cells were also acquired using a Zeiss LSM i880.

Analysis of HA Synthesis

Control and lentiviral transduced MCF10A and primary equine synoviocytes were plated and induced with 0.2 µg/mL doxycycline (Santa Cruz) for 24 h. Total levels of HA secreted into the cell culture media were measured via the DuoSet Hyaluronan ELISA kit following manufacturer's protocol. Briefly, a 96-well microplate was coated with recombinant human Aggrecan. HA in cell culture media was captured by the coated Aggrecan and detected with Biotin-HABP/HRP-Streptavidin. HA concentration was measured using S. pyogenes HA standard (R&D Systems).

Analysis of HA Molecular Size

HA molecular mass was assayed by electrophoresis and blot analysis essentially as described (Yuan et al., 2013), using agarose instead of polyacrylamide for gel electrophoresis. Briefly, cell culture media containing HA was loaded in a 0.6% agarose gel in Tris/Borate/EDTA (TBE) buffer. Following electrophoresis, samples were transferred to HyBond N+ membrane (GE Healthcare). HA was probed with biotin-HABP (0.125 μg/ml in 0.1% BSA-PBS, 1 h) and subsequently detected with HRP-Streptavidin (0.025 µg/ml in 0.1% BSA-PBS, 1 h). Blots were developed in ECL substrate (Amresco), imaged on a ChemiDoc (BioRad) documentation system, and quantified in ImageJ Fiji (Schindelin et al., 2012).

Cancer Cell Line Sorting

MCF10A wild-type (Control) or Muc1-42TR ΔCT-expressing cells and cancer cell lines (T47D, ZR-75-1, HeLa) were plated at 10,000 cell/cm² overnight. MCF10A cells were induced with 0.2 µg/mL doxycycline (Santa Cruz) for 24 h. Cell lines were non-enzymatically detached using 1 mM EDTA in PBS. Detached cells were washed with 0.5% BSA in PBS. For each cell line, FITC-conjugated anti-Muc1 antibody was diluted 1:500 per million cells and incubated with cells on ice for 30 min. Cells were washed with 0.5% BSA in PBS three time before sorting. Cells were sorted with a BD FACS Aria II onto poly-I-lysine treated 8 mm coverslips at 2,000 to 5,000 cells/cm² for SEM, allowed to adhere for 4 h at 37°C, and fixed for SEM imaging.

Analysis of Mucin Radius of Gyration

The Muc1 polymer domain with 42 tandem repeats (S6 Muc1-42TR 10xHis) was produced recombinantly in suspension adapted Freestyle 293-F cells. Stable Freestyle 293-F cell lines were prepared with the Muc1-42TR 10xHis pPB tetOn PuroR as described above. Production of Muc1 biopolymer was induced with 1 µg/mL doxycycline (Santa Cruz) in 30 mL of suspension culture in Freestyle 293-F media. Induced media was collected after 24 h and purified on HisPur Ni-NTA resin (Thermo Fisher) according to standard protocols. Briefly, 1 mL bed volume of Ni-NTA resin was rinsed with equilibration buffer (20 mM sodium phosphate, 0.5 M NaCl, pH = 7.4). Equilibrated resin was incubated overnight at 4°C with 10 mL harvested Freestyle 293-F media diluted in 30 mL of equilibration buffer. Beads were washed in equilibration buffer with 5 mM imidazole and eluted in equilibration buffer with 500 mM imidazole. Eluted protein was dialyzed against PBS and analyzed by SDS-PAGE. Gels were stained with SYPRO Ruby Protein Gel Stain (Thermo Fisher) according to manufacturer's instructions to confirm protein size and purity. Gels were blotted and probed with Muc1 and His antibodies to confirm mucin identity and PNA lectin to confirm mucin O-glycosylation. Purified recombinant Muc1 was dialyzed against PBS to remove imidazole.

The radius of gyration of the recombinant Muc1 polymer domain was measured with size-exclusion chromatography-coupled to multiangle light scattering (SEC-MALS). Purified protein (40 μ L of Muc1 with a concentration of 5 μ g/ μ L) was subjected to SEC using a Superdex 200 Increase 10/300 column (GE Healthcare) equilibrated in MALS buffer (20 mM sodium phosphate, 0.5 M NaCl, pH 7.4). The SEC was coupled to a static 18-angle light scattering detector (DAWN HELEOS-II) and a refractive index detector (Optilab T-rEX, Wyatt Technology). Data were collected every second at a flow rate of 0.7 mL/min. Data analysis was carried out using ASTRA VI, yielding the radius of gyration of the sample (32.0 nm \pm 0.4%). For normalization of the light scattering detectors and data quality control, monomeric BSA (Sigma) was used.

Variation of Mucin Size and Surface Densities Mucin Lengths

MCF10As expressing Muc1 GFP-ΔCT with 0, 10, or 42 tandem repeats were sorted for similar levels of GFP on a BD FACs Aria II using the Muc1 antibody first for the 42 tandem repeat population then the GFP nanobody Atto 647N (Chromotek) for the 0, 10, and 42 tandem repeat populations. Stable populations were created from these sorted lines. Cells were plated onto 8 mm coverslips at 10,000 cells/cm² for 16-18 h, then induced with 0.2 μg/mL of doxycycline (Santa Cruz) for 24 h and fixed for SEM analysis.

Mucin Cell Surface Density

Using the GFP nanobody with an approximate size of 2 nm (15 kDa) and picomolar affinity for GFP (GFP Binding Protein, Chromotek) and labeled with NHS-Alexa Fluor 647 according to manufacturer's protocol, 647-nanobody, MCF10A cells expressing Muc1-42TR GFP Δ CT were labeled in 5 μ g/ml 647-nanobody for 20 min on ice to label only cell surface mucins. Cells were sorted with a BD FACS Aria II onto poly-I-lysine (Trevigen/Cultrex) -treated 8 mm coverslips at 5,000 to 10,000 cells/cm² for SEM, allowed to adhere for 4 h at 37°C, and fixed for SEM imaging. Alternatively, cells were sorted with a BD FACS Aria II into 1.7 mL Eppendorf tubes, resuspended in 100 μ L 0.5% BSA in PBS, and lysed with 100 μ L 2X RIPA lysis buffer for estimation of mucin surface densities via SDS-PAGE. Lysed samples were run simultaneously with 647-nanobody standards of known molecular concentration. 647-nanobody fluorescence in lysed samples and standards were imaged on a Typhoon 9400 imaging system (GE Healthcare). Total fluorescence in each sample or standard was quantified in ImageJ Fiji (Schindelin et al., 2012). A standard curve was constructed by relating fluorescence from nanobody standards to their known concentration. The number of labeled mucins in each lysate were estimated based on the standard curve. The mucin surface density was estimated by dividing the total number of mucins by the known number of cells in each sample and their average surface area of 5,000 μ m² based on an average radius of 20 μ m and spherically shaped wild-type cells in suspension. A standard curve was constructed based on the number of mucins per area and the known mean fluorescence signal from the FACS collected population. This standard curve was then applied to calculate the number of mucins per area of populations collected subsequently.

Expansion Microscopy

Expansion microscopy (ExM) was performed as described previously (Tillberg et al., 2016) and involved steps of anchoring fluorescent dyes and proteins, gelation, digestion, and expansion to achieve dye retention and separation. Briefly, fixed and stained cells were anchored with 0.1 mg/ml Acryloyl-X, SE (6-((acryloyl)amino)hexanoic acid, succinimidyl ester (ThermoFisher) in PBS for 16 h at RT, washed twice and further incubated 1 h at 37°C in a monomer solution (1 \times PBS, 2 M NaCl, 8.625% (w/w) sodium acrylate, 2.5% (w/w) acrylamide, 0.15% (w/w) N,N'-methylenebisacrylamide) mixed with ammonium persulfate 0.2% (w/w) initiator and tetramethylethylenediamine 0.2% (w/w) accelerator for gelation. For digestion, gelled samples were gently transferred into 6 well glass bottom plates (Cellvis) and treated with Proteinase K (New England Biolabs) at 8 units/mL in digestion buffer (50 mM Tris (pH 8), 1 mM EDTA, 0.5% Triton X-100, 1 M NaCl) for 16 h at room temperature. For expansion, digested gels were washed in large excess volume of ddH₂O for 1 h. This was repeated 4–6 times until the expansion plateaued. Samples were imaged on a Zeiss LSM inverted 880 confocal microscope using a 40x water immersion objective (NA 1.1) in Airyscan mode to optimize resolution.

Isolation of Extracellular Vesicles

Cell were plated at 10,000 cells/cm 2 in appropriate dishes. Following induction with 1 μ g/ml doxycycline (Santa Cruz) for 18 h, cells were rinsed with PBS twice then serum-starved for an additional 6 h with 1 μ g/mL doxycycline (Santa Cruz). For actin depolymerization studies, cells were treated for 60 min with 10 μ M LatA (Cayman Chemical) in serum free media prior to isolation. For HAS3 digestion studies, cells were treated with 1 U/mL hyaluronidase for 60 min in serum-containing media before 6 h subsequent treatment in serum-starved media. For HeLa experiments, cells were sorted for high and low mucin expression and then immediately rinsed 2X in serum free media and spun at 200 x g for 5 min before 6 h serum starvation in the presence of 0.1 μ g/mL EGF for microvesicle stimulation. Conditioned media from serum-starved cells was clarified by pelleting cellular debris through two consecutive centrifugations at 600 x g for 5 min.

Plunge-Freezing Vitrification

From clarified media, 3–5 μ L of sample was pipetted onto holey carbon-coated 200 mesh copper grids (Quantifoil Micro Tools, Jena, Germany) with hole sizes of \sim 2 μ m. The grids were blotted from the reverse side and immediately plunged into a liquid ethane/propane mixture cooled to liquid nitrogen temperature using a custom-built vitrification device (MPI, Martinsried, Germany). The plunge-frozen grids were stored in sealed cryo-boxes in liquid nitrogen until used.

Cryogenic Transmission Electron Microscopy

Cryogenic transmission electron microscopy (cryo-TEM) was performed on a Titan Themis (Thermo Fisher Scientific, Waltham, MA) operated at 300 kV in energy-filtered mode, equipped with a field-emission gun, and 3838x3710 pixel Gatan K2 Summit direct

detector camera (Gatan, Pleasanton, CA) operating in Counted, dose-fractionated modes. Images were collected at a defoci of between -1 µm and -3 µm. Images were binned by 2, resulting in pixel sizes of 0.72–1.1 nm.

Theoretical Model Details Glycocalyx Polymer Brush Model

We propose a simple model to explain how biopolymers in the glycocalyx can generate entropic driving forces for membrane curvature. The model considers long chain polymers anchored on one end to the plasma membrane. Common examples of long-chain polymers in the glycocalyx include mucins and hyaluronic acid (HA), which we model specifically here. The modeling framework could be similarly applied to other types of glycocalyx polymers, including polysialic acid and other glycosaminoglycans. Hyaluronic acid is a semi-flexible linear polysaccharide comprised of repeating units of glucuronic acid and N-acetylglucosamine. Mucins have a more complex bottlebrush structure comprised of a central polypeptide backbone and densely clustered glycan side chains along the backbone. Although their structure is complex, bottlebrush polymers can be modelled as effective linear polymers with a monomer size on the order of the side chains (Paturej et al., 2016). Therefore, we consider all glycocalyx polymers in our model to be linear or effectively linear.

Biopolymers in the glycocalyx are anchored to the cell surface in several ways, including through transmembrane anchors, covalent conjugation to integral membrane proteins, and non-covalently to specific transmembrane receptors. Cell surface mucins are anchored directly near their carboxy terminus by a single transmembrane domain. Hyaluronic acid is anchored to the cell surface through specific transmembrane receptors on the cell surface. While it is possible for hyaluronic acid to be anchored at multiple points along the polymer backbone, for simplicity, we consider all glycocalyx polymers to have a single membrane anchor at one end.

The cell surface is also decorated with many types of integral and peripheral membrane proteins. These molecules could also contribute to an entropic pressure on the cell membrane, similar to a 2D gas pressure. To isolate the effects of glycocalyx polymers on the membrane, we neglect possible contributions from other cell surface proteins, as well as intracellular forces. However, the model could be extended to include these additional contributions to the system energy.

Biopolymers have excluded volumes accounting for steric interactions between monomers on the same polymer as well as between monomers on adjacent molecules (de Gennes, 1980). Large negative charges on acidic sugars, such as glucuronic acid and sialic acid, give rise to intramolecular and intermolecular electrostatic interactions (Israels et al., 1994). Finally, the polymers and the brush have entropic contributions due to the elastic energy, which captures the stretch of the molecules (de Gennes, 1980). Embedded in a deformable lipid membrane, the energy of this polymer glycocalyx and that of the membrane can minimize to yield the equilibrium configuration (Lipowsky, 1995; Stachowiak et al., 2012). Hence, in our model below, we perform an energy minimization of the glycocalyx and the underlying membrane to describe the surface curvature.

Depending on surface density, polymers tethered to a surface exhibit two particular regimes of physical behavior – mushroom and brush. The Flory radius measures the approximate size of an entire polymer, and is given by $R_F \approx l_a N_a^\nu = l^\nu l_a^{1-\nu}$, where l_a is the size of each monomer or effective monomer, N_a is the number of such monomers in a polymer, l is the fully extended length of the polymer chain, and ν is called the Flory exponent. $\nu \cong 0.6$ for hydrophilic biopolymers in good solvents like water. At low densities, such that intermolecular spacing is larger than the polymer Flory radius, i.e. $C_G < 1/(R_F)^2$, where C_G is biopolymer concentration, biopolymers take up preferable conformations independent of neighbor interactions. In this regime, the flexible molecules can coil up to exhibit mushroom-like structures. On the other hand, at high surface concentrations, when the intermolecular spacing is smaller than the Flory radius, intermolecular interactions can dominate and stretch the biopolymers out into a brush-like structure. The polymer layer extension or thickness, the stored energy, and the generated membrane curvatures exhibit different scaling laws in these regimes, as described below.

In the mushroom regime, the attachment of a biopolymer to a flat, impenetrable surface reduces the number of accessible molecular conformations relative to those of a polymer free in solution. Attachment to a substrate eliminates polymer shapes that would have to penetrate the surface. Curving the impenetrable grafting surface can free up space for the polymer, marginally increasing the permissible configurations and the entropy of the polymer. Thus, flexible biopolymers tethered to a deformable membrane can generate curvatures, as described by Lipowsky (Lipowsky, 1995). However, the additional entropy due to membrane curvature is small and consequently, curvatures generated by polymer mushrooms are also small, relative to deformations elicited by intermolecular interactions in polymer brushes. In this mushroom regime, the free energy due to the entropic contribution of each mushroom polymer tethered to a curved membrane is:

$$F_{mushroom} = -TS_{mushroom} \sim -k_B T \frac{2\pi R_{mushroom}}{R}, \tag{1}$$

where the reference configuration is the polymer tethered to a flat surface, $S_{mushroom}$ is the corresponding entropic contribution, $R_{mushroom}$ is the Flory radius of the mushroom-shaped biopolymer, and R is the radius of curvature of the underlying membrane. In the mushroom regime, we consider the formation of spherical membrane structures. The bending energy of the curved membrane is:

$$F_{membrane} = \frac{\kappa}{2C_G R^2},\tag{2}$$

where κ is the bending stiffness of the membrane bilayer, C_G is the surface density of the biopolymers, and $1/C_G$ is the area available for each polymer. Minimizing the total energy, $F_{total} = F_{mushroom} + F_{membrane}$ with respect to the radius of curvature, R, as $\partial F_{total}/\partial R = 0$, we obtain the following scaling law for R:

$$R \sim \frac{\kappa}{k_B T} \frac{1}{2\pi C_G I_s N_s^s},\tag{3}$$

where I_a is the size of a monomeric segment and N_a is the number of such segments in a polymer.

At high surface densities, such that neighboring polymer molecules interact with each other, grafted polymers exhibit a brush-like structure (de Gennes, 1980). Intermolecular steric and electrostatic interactions are significantly higher in this regime, implying the creation of higher curvature-generating forces. In this regime, we consider the formation of tubular structures from the membrane and predict the tubule curvatures generated by intermolecular crowding effects on the cell surface. An energy minimization approach elucidates the equilibrium curvature and brush extension as follows. For a tubule with radius *R*, the energy of the glycocalyx per length of the tubule contains elastic, excluded volume, and electrostatic components (Borisov and Zhulina, 2002; Bracha et al., 2013; Zhulina et al., 2006):

$$F_{brush} = F_{elastic} + F_{excluded \ volume} + F_{electrostatic}, \tag{4}$$

$$F_{brush} = k_B T \int_{B}^{B+H} \left[\frac{3}{2I_a^2 c_p s} + \left(w + \frac{\alpha_b^2}{2\Phi_{ion}} \right) c_p^2 s \right] dr, \tag{5}$$

where R is the radius of the tubule, H is the thickness of the glycocalyx brush, I_a is the size of monomeric segments that form the biopolymers, c_p is the monomer concentration, and s is the area per polymer. At the tubule surface, the area per polymer, s(r=R) is related to the biopolymer surface density, C_G , as $s(r=R)=1/C_G$. w is the excluded volume of monomer segments, α_b is the degree of ionization of a monomer, Φ_{ion} is the ion concentration in bulk solution, and r is a radial coordinate.

Zhulina et al. (Zhulina et al., 2006) provide expressions for c_p . Given the monomer length and diameter are similar (Paturej et al., 2016), we consider the monomeric segments to be cylinders with an aspect ratio close to 1. The energy per length of the underlying membrane bent into the tubular structure is (Helfrich, 1973):

$$F_{membrane} = \frac{\pi \kappa}{R},\tag{6}$$

where κ is the membrane bending modulus. Thus, the total energy per tubule length is:

$$F_{total} = F_{brush} + F_{membrane} = k_B T \int_{R}^{R+H} \left[\frac{3}{2l_a^2 c_p s} + \left(w + \frac{\alpha_b^2}{2\Phi_{lon}} \right) c_p^2 s \right] dr + \frac{\pi \kappa}{R}.$$
 (7)

Minimizing the total energy with respect to the tubule radius $(dF_{total}/dR = 0)$ reveals the dependence of the spontaneous curvature on the properties of the glycocalyx and the cell membrane, including the surface density of biopolymers.

We consider the implications of this theory for native Muc1, as an example mucin. We course-grain the bottlebrush biopolymer into N_a effective monomers of size $I_{a, eff}$ (Paturej et al., 2016). In this work, we measure the radius of gyration, R_G , of Muc1 to be 32 nm. We estimate the overall stretched length, I, to be 270 nm based on electron micrographs of Muc1 purified from human HEp-2 epithelial cells (Bramwell et al., 1986). The radius of gyration is related to the Flory radius by $R_G \approx (1/\sqrt{6})R_F = (1/\sqrt{6})I^\nu I_{a,eff}^{1-\nu}$. Using estimates of $R_G = 32$ nm, I = 270 nm, and $\nu = 0.6$, we estimate the mucin to be described by $N_a = 18$ effective monomeric segments each having a size of $I_{a,eff} = 15$ nm. We note that this effective monomer size is in good agreement with expectations based on estimates of the mucin side chain size to be 5-10 nm (Kesimer et al., 2013; McMaster et al., 1999). We assume that sialic acids on mucins contribute to a charge density of approximately $5 \, \mathrm{e^-}$ per 20 amino acid tandem repeat. Our assumption is based on most mucin O-glycosylation sites being occupied with sialylated glycans (Bäckström et al., 2003; Müller et al., 1999).

The scaling law for the mucin mushroom regime predicts small spontaneous curvatures for low biopolymer densities (Figure 4C). The predicted spontaneous curvatures are comparable to the curvatures of the bleb-like protrusions observed in cells expressing low surface densities of mucins, as shown in Figure 5B, 180 mucins/ μ m². For higher densities, where the biopolymers form a brush, the corresponding model above predicts the generation of curvatures similar or greater to those observed in the tubules on the cells of Figure 5B, 52,000 mucins/ μ m². The curvature of such tubules is predicted to increase exponentially with biopolymer density. Notably, the continuous transition between mushroom and brush regimes predicted about a biopolymer density of 250 #/ μ m² accompanies a change in cell surface morphology from bleb-like to tubulated (Figures 5B, 5D, and 5E).

Similarly, HA molecules closely resemble linear polymer chains. For instance, a 1 MDa HA molecule has a length of 2.5 µm when stretched out and can be modeled as a chain of 250 monomeric units approximately 10 nm long (Cleland Robert, 2004; Hayashi et al., 1995). Polymer theory predicts such a polymer to have a large Flory radius of about 1 µm, which is more than an order of magnitude larger than that of Muc1. Thus, HA is expected to have a much larger effective volume and physical presence on the cell surface than

Muc1. The consequently stronger intramolecular and intermolecular interactions in HA should render it significantly more effective at bending the membrane than Muc1. Consequently, considerably lower surface density of HA is expected to generate the same membrane curvature as a surface densely crowded with Muc1.

We also conducted preliminary calculations for the specific example of HA. Adopting the approach of Bracha et al. on DNA, also a linear polyelectrolyte, we coarse grained hyaluronic acid into N_a cylindrical segments of length I_a and diameter d to allow application of polymer brush theory scaling laws (Bracha et al., 2013). The Kuhn length, l_a , of the biopolymers is twice the persistence length and the length scale at which the molecule is straight. Hyaluronic acid is semi-rigid owing to the local stiffness that arises from intrinsically large size of the sugar ring monomers and the hindered rotations about the glycosidic linkages (Day and Sheehan, 2001). Measurements of the persistence length range from 5 to 9 nm. The diameter of the hyaluronic acid chain is about 0.6 nm (Cowman et al., 2005). In this work, we measure the molecular weight of hyaluronic acid produced by the hyaluronic acid synthase 3 (HAS3) to be approximately 3 MDa. This large size corresponds to a fully stretch length of approximately 10 μm, assuming a disaccharide size of 1 nm. Force Requirements for Cell Surface Blebs and Tubes

To predict the relative frequencies of blebs and tubes on the cell surface, we perform energetic calculations for the cell membrane. The crowding pressure of the glycopolymers effectively increases the natural curvature of the cell membrane. Hence, we lump together the crowding effects of the glycocalyx into a spontaneous membrane curvature, c₀.

Intracellular forces pushing the cell membrane out, e.g. actin polymerization, can generate cylindrical tubes (Weichsel and Geissler, 2016). Here we consider a tube of length L and radius R_{tube} generated due to a force f. On the other hand, a hydrostatic pressure difference p between inside and outside the cell can form spherical blebs of radius R_{bleb} (Charras and Paluch, 2008). The energy of the membrane in these configurations includes the bending energy, surface tension, and contributions from the pressure p or the force f (Derényi et al., 2002; Helfrich, 1973; Seifert et al., 1991):

$$F = \int_{A}^{\kappa} \frac{(c_1 + c_2 - c_0)^2 dA + \sigma A - \rho V - fL,}{(8)}$$

where κ is the bending stiffness of the membrane, c_1 and c_2 are the principal curvatures, c_0 is the spontaneous curvature of the membrane – generated due to the crowding pressure of the biopolymers, A is the area of the membrane, and σ is the surface tension of the membrane. For tubes, p = 0, $f \neq 0$, and L is the length of the tube, whereas for blebs, f = 0, $p \neq 0$, and V is the bleb volume.

A cylindrical tube of radius R_{tube} has spontaneous curvatures, $c_1 = 0$ and $c_2 = 1/R_{tube}$, which simplify the energy:

$$F_{tube} = \left[\frac{\kappa}{2} \left(\frac{1}{R_{tube}} - c_0\right)^2 + \sigma\right] 2\pi R_{tube} L - fL. \tag{9}$$

The case of a spherical bleb with a very thin neck provides an upper limit on the energy of a bleb. For a bleb with radius R_{bleb} , $c_1 =$ $c_2 = 1/R_{bleb}$, and

$$F_{bleb} = \left[\frac{\kappa}{2} \left(\frac{2}{R_{bleb}} - c_0 \right)^2 + \sigma \right] 4\pi R_{bleb}^2 - \frac{4\pi R_{bleb}^3}{3} p. \tag{10}$$

At equilibrium, these energies are minimized with respect to the radii of the blebs and tubes (Derényi et al., 2002). The tube energy is also minimized with respect to the tube length L at steady state (Derényi et al., 2002). That is,

$$\frac{\partial F_{tube}}{\partial R_{tube}} = 0, \quad \frac{\partial F_{tube}}{\partial L} = 0, \tag{11}$$

and

$$\frac{\partial F_{blob}}{\partial R_{blob}} = 0 \tag{12}$$

at equilibrium. The equilibrium equations (Eq. 11) for the tube imply:

$$R_{tube} = \frac{1}{\sqrt{c_0^2 + 2\sigma/\kappa}},\tag{13}$$

and

$$f = 2\pi\kappa \left(\sqrt{c_0^2 + 2\sigma/\kappa} - c_0 \right). \tag{14}$$

These equilibrium calculations predict the tube radius is completely governed by the mechanical properties of the lipid bilayer and the spontaneous curvature, which in this case is generated by intermolecular interactions in the glycocalyx brush. These calculations do not account for the structural support of actin filaments widening the tubes.

Bleb energy minimization (Eq. 12) yields the pressure requirement for a bleb of a given size:

$$\rho = \frac{2\sigma}{R_{bleb}} - \frac{c_0 \kappa}{R_{bleb}} \left(\frac{2}{R_{bleb}} - c_0 \right). \tag{15}$$

Eq.13-15 relate the force or pressure required to maintain a tube or bleb with the spontaneous curvature generated by the biopolymers. Figure 4C details the dependence of the spontaneous curvature on biopolymer concentration. We thus graph the force and pressure requirements against the biopolymer concentration (Figure 4D). Comparisons with typically observed forces from actin polymerization and hydrostatic pressures explain the relative densities of tubes and blebs as a function of biopolymer density.

QUANTIFICATION AND STATISTICAL ANALYSIS

Scanning Electron Microscopy Quantification

Cellular tube density, diameter, and length were analyzed in ImageJ Fiji (Schindelin et al., 2012). For quantification of tube density per area, a \sim 2 μ m × 2 μ m region of interest was drawn, and the encompassed tubes counted manually using the cell counter plug-in. Tube diameter was measured by drawing a straight line through the tube cross section at its mid-point. Tube length was measured for tubes extending approximately parallel to the image plane, as identified by visual inspection, using the ImageJ line segment tool.

Giant Unilamellar Vesicles Quantification

Dye fluorescent intensity was measured by taking 5 different line scans across the GUV in ImageJ Fiji (Schindelin et al., 2012). The intensity profile of each line was analyzed using Mathematica 10.3, where the integral of the intensity peak was calculated and averaged for 5 different lines per GUV.

Nanoparticle Tracking Analysis

Extracellular vesicles in the clarified media were analyzed using a Malvern NS300 NanoSight. Imaging was performed for 60 s with five captures per sample. Particle analysis was performed using Malvern Nanoparticle Tracking Analysis software.

Expansion Microscopy Quantification

Line profiles across membrane tubules in expansion images were used to measure the separation of GFP nanobody fluorescence from SUMO fluorescence. Brush height was determined by the difference of the full width at half maxima (FWHM) between GFP nanobody fluorescence and SUMO fluorescence.

Statistics

Statistics were calculated in Graphpad Prism. One-way ANOVA and post-hoc two-tailed Student's t test were used where appropriate as indicated by figure legends. For boxplots - center lines show the medians; box limits indicate the 25th and 75th percentiles as determined by BoxplotR software; whiskers extend 1.5 times the interquartile range from the 25th and 75th percentiles, and notches, where shown, indicate the 95% confidence interval. See individual figure legends for number of replicates and statistical testing details. ns - not significant; */+ p < 0.05; **/++ p < 0.01; ***/+++ p < 0.001.

DATA AND SOFTWARE AVAILABILITY

Authors will provide all raw images and programming scripts upon request. All cDNAs will be made available through the Addgene repository or through direct request to M.J.P. upon publication of the manuscript.

Supplemental Figures

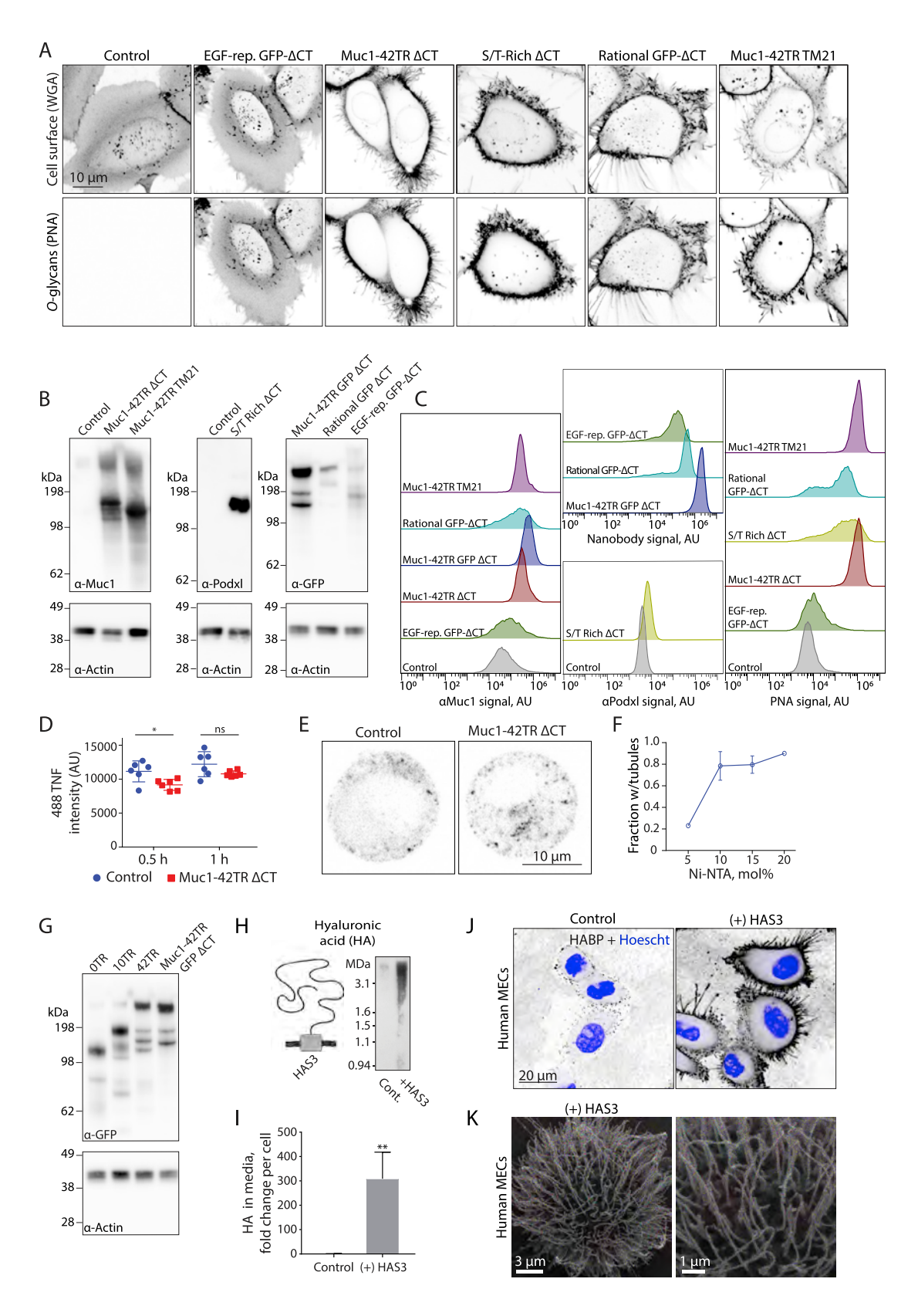


Figure S1. Validation of Genetically Encoded Mucins, Related to Figure 1

- (A) Representative confocal microscopy images showing membrane tubularization induced by various engineered glycoproteins compared to wild-type (Control) cells. The cell surface is visualized with lectin WGA (wheat germ agglutinin). Mucin staining with lectin PNA (peanut agglutinin) confirms glycoprotein O-glycosylation and surface localization on MCF10A cells. Images are individually adjusted for contrast, n = 2.
- (B) Representative western blots showing the relative size of various transmembrane biopolymers compared to each other biopolymer and the endogenous Muc1 in wild-type (Control) cells, n = 3.
- (C) Representative flow cytometry histograms showing the cell surface level of various transmembrane biopolymers, >2,000 cells per population, n = 3.
- (D) Quantification of endocytosis of Alexa Fluor 488 labelled transferrin (488 TNF) after 0.5 or 1 h of treatment. Quantification performed with flow cytometry, median signal reported with background subtraction, >10,000 cells per population, n = 6, error bars are SD.
- (E) Representative confocal microscopy images of endocytosed 488 TNF after 0.5 h of treatment.
- $(F) \ Quantification \ of \ the \ fraction \ of \ GUVs \ with \ Podocalyxin \ tethered \ to \ the \ surface \ with \ visible \ membrane \ tubularization, \ n=25.$
- (G) Western blot showing polymer sizes expressed in epithelial cells, analyzed with an antibody against the green fluorescent protein (GFP) tag, n = 5.
- (H) (Left) Cartoon of hyaluronic acid (HA) extruded by the transmembrane protein hyaluronic acid synthase 3 (HAS3). (Right) Blot of HA in lysates of wild-type (Cont.) and hyaluronic acid synthase 3 (HAS3)-expressing human mammary epithelial cells (MECs, MCF10A). Note that the expressed HA is a giant linear polymer in the MDa range.
- (I) ELISA quantification of HA secreted by MECs into their media, normalized to the number of cells in the sample and the HA secretion of Control cells, n = 3. Data show ean + SD
- (J) Representative confocal microscopy images of human MECs, either wild-type (Control) or stably expressing HAS3. Cells are stained with Hoescht (nucleus) and Alexa Fluor 568 hyaluronic acid binding protein (HABP).
- (K) Representative SEM images showing highly elongated membrane tubules in HAS3-expressing human MECs (left) and a zoomed in region on the same cell (right).
- ns, not significant; *p < 0.05, **p < 0.01, ***p < 0.001 (post-hoc Student's two-tailed t test).

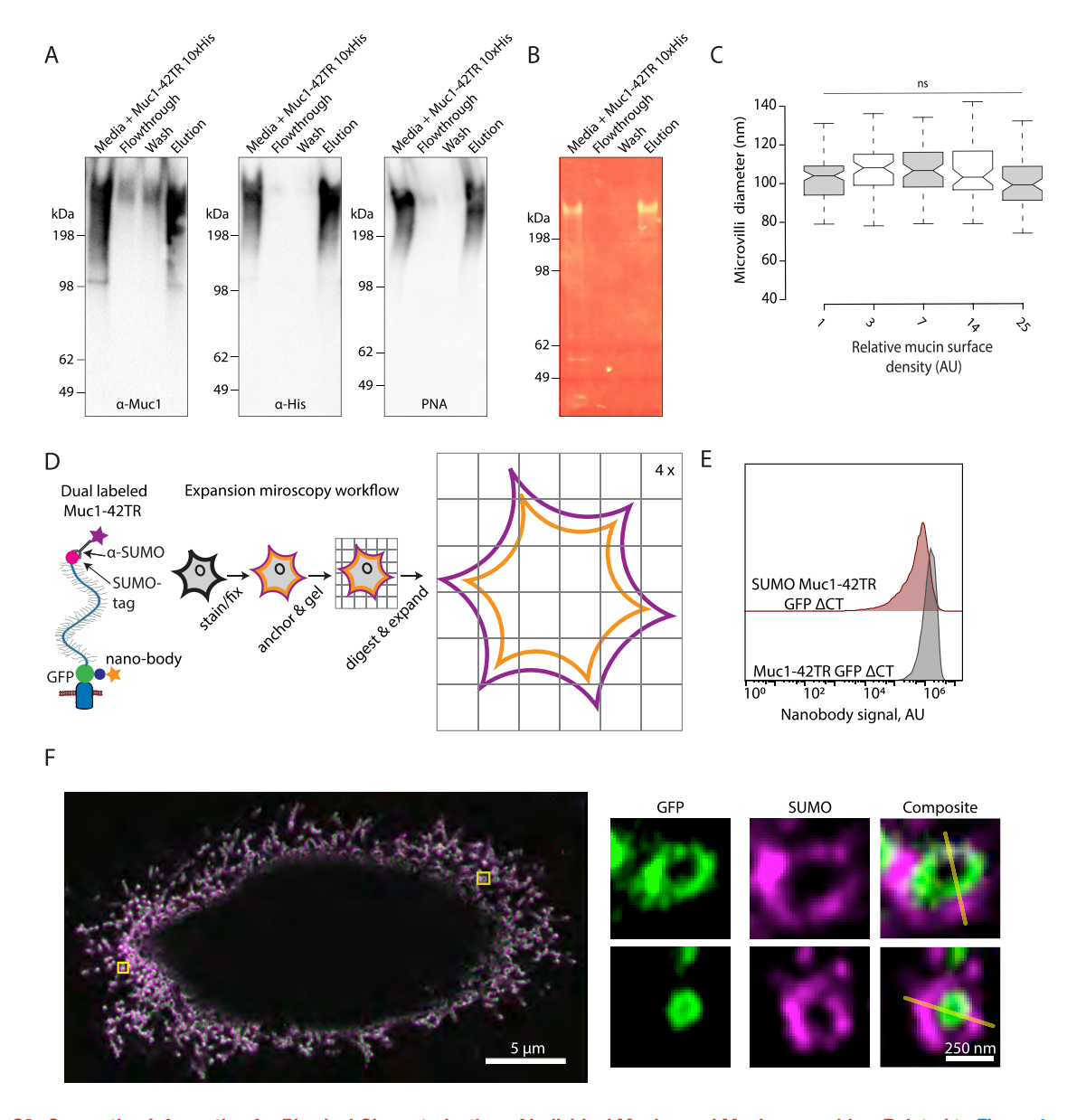


Figure S2. Supporting Information for Physical Characterization of Individual Mucins and Mucin ensembles, Related to Figure 4

(A) Western blot validation of recombinant Muc1-42TR production (Media + Muc1-42TR 10xHis), Ni-NTA resin binding of the protein (Flow-through), wash off non-specific proteins (Wash), and purified recombinant Muc1-42TR polymer (Elution). Samples are probed with anti-Muc1 and anti-His antibodies as well as PNA (peanut agglutinin) to bind O-linked glycans.

- (B) SYPRO Ruby protein gel stain for samples described above.
- (C) Quantification of epithelial microvilli diameter for the indicated relative mucin surface densities. Box notches indicate 95% confidence intervals.
- (D) (left) Mucin construct (Muc1-42TR) with SUMO and GFP tags flanking the polymer domain for visualization of polymer extension with expansion microscopy (ExM). (Right) ExM sample workflow. First, samples are stained and fixed. Then the proteins are chemically linked (anchored) to monomers which polymerize to form a gel. Proteins are then digested, and the gel is expanded to four times the original size.
- (E) Representative flow cytometry histogram showing the geometric mean of GFP nanobody binding for the indicated biopolymers. The two polymers are expressed on the cell surface at comparable levels, >14,000 cells per population, n = 3.
- (F) (Left) Representative ExM image with two regions of interest on the cross-section of microvilli indicated by yellow boxes. (Right) Zoomed in regions of interest. Yellow line composite image represents a line trace which may be used to calculate the full-width half max value for the GFP nanobody and SUMO antibody signals to calculate the cell surface brush height. ns, not significant.

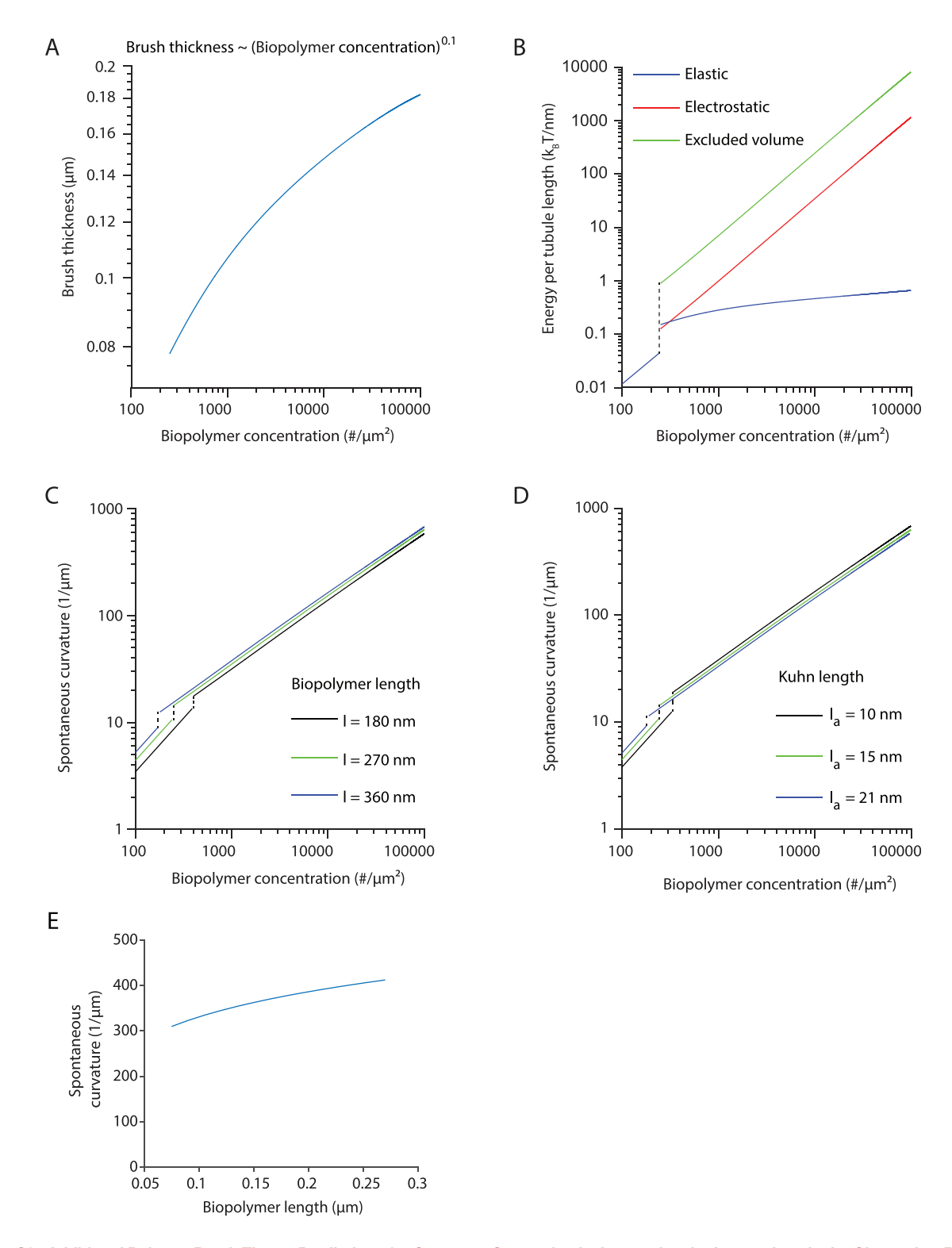


Figure S3. Additional Polymer Brush Theory Predictions for Curvature Generation by Intermolecular Interactions in the Glycocalyx, Related to Figure 4

(A) Graph for the predicted brush thickness as a function of biopolymer surface density in the brush regime. Brush thickness scales approximately as a power law with biopolymer concentration.

(B) Plot showing energetic contributions as functions of the biopolymer density. In the mushroom regime, polymers have only elastic energy, while in an extended brush, excluded volume and electrostatic interactions contribute to biopolymer free energy.

⁽C) Plot depicting variation of spontaneous curvature generated with biopolymer density and molecular length.

⁽D) Graph displaying trend of spontaneous curvature as a function of biopolymer density and Kuhn length. Kuhn length, equal to twice the persistence length, is directly proportional to polymer bending stiffness, and is referred to as the length of a monomeric segment in the manuscript.

Plots in (A–D) are in log-log format. Plots in (A) and (B) use biopolymer length, I = 270 nm, and monomeric segment length, $I_a = 15$ nm. Plot (C) employs polymer monomer segment size of 15 nm, and (D) uses biopolymer length of 270 nm.

⁽E) Predicted dependence of spontaneous curvature on biopolymer length at high density. This graph uses polymers of $l_a = 15 \, nm$ packed at a density of 50000 $\#/\mu m^2$.

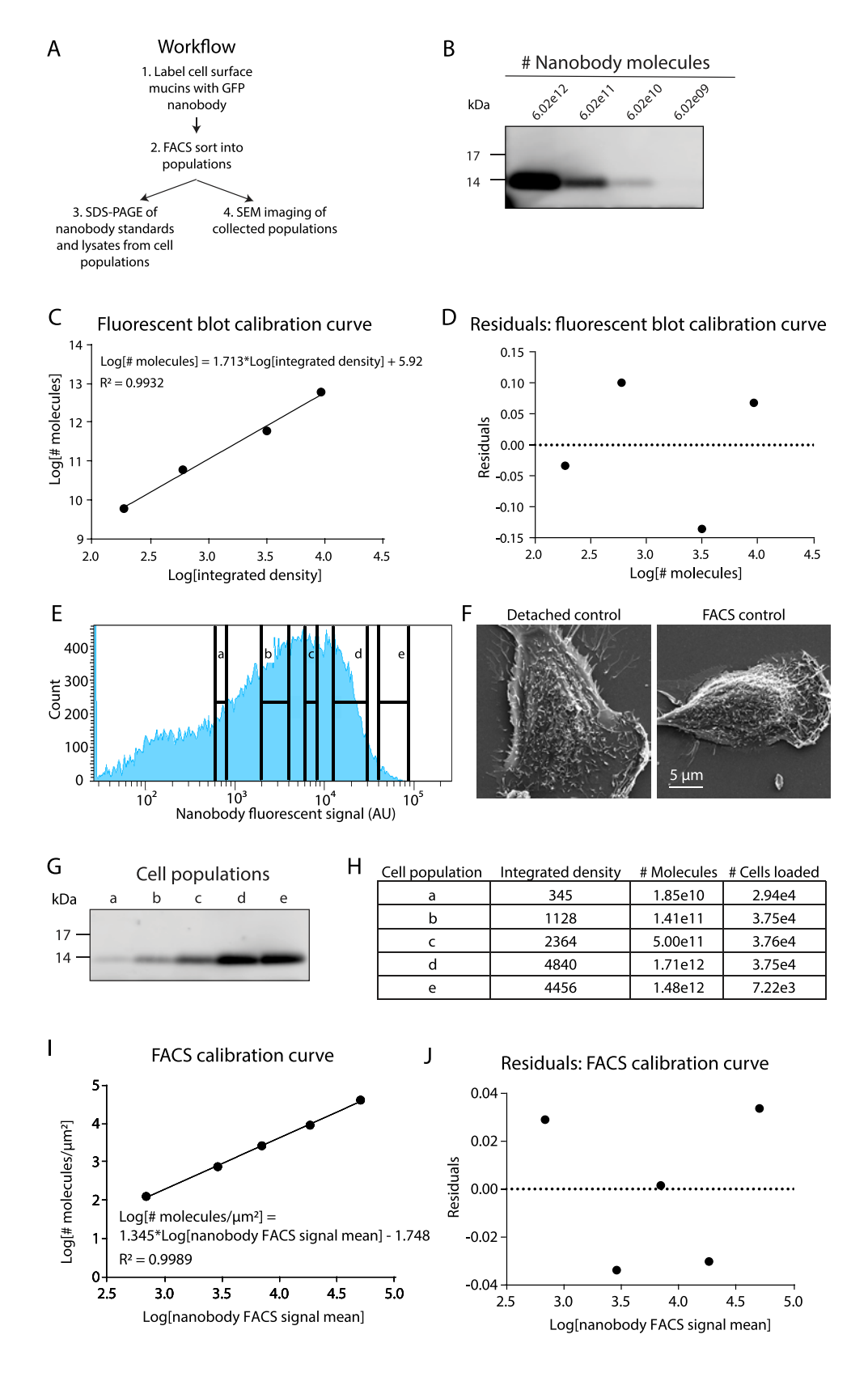


Figure S4. Fluorescence-Activated Sorting and Quantification of Muc1 Surface Densities, Related to Figure 5

- (A) Extended workflow for quantitative experiments at different Muc1 surface densities.
- (B) SDS-PAGE calibration of Alexa Fluor 647 labeled nanobody.
- (C) Calibration curve between the log value for integrated density of fluorescence signal from nanobody dilution series (shown in (B)) versus the log value of the number of molecules loaded. A linear regression fit and R² value are shown.
- (D) Residuals for the linear regression fit shown in (C).
- (E) Fluorescence-activated cell sorting (FACS) histogram showing the nanobody fluorescence signal and the populations 'a' through 'e' collected for these experiments.
- (F) Representative scanning electron microscopy (SEM) images of wild-type cells which were non-enzymatically detached from the substrate then re-adhered (detached control) for SEM imaging and cells which were non-enzymatically detached from the substrate, collected through the FACS, then re-adhered (FACS control). These images demonstrate that the method of FACS collection did not influence the membrane shapes observed with Muc1-42TR ΔCT expression (shown in Figure 1G).
- (G) SDS-PAGE analysis of fluorescent nanobody signal in each cell population, a-e, after collection and lysis of the cells.
- (H) Table describing the integrated density signal from the fluorescence image shown in (G), the calculated number of molecules based on the calibration curve in (C), and the number of cells loaded in the protein gel, (G), based on the number of cells collected with FACS for each population, (E).
- (I) Calibration curve between the log of the nanobody mean signal from the FACS versus the number of molecules calculated for each population. The number of molecules per sample was normalized by the number of cells loaded and the approximate area per cell. Linear regression fit and R^2 values shown.
- (J) Residuals for linear regression fit shown in (I).

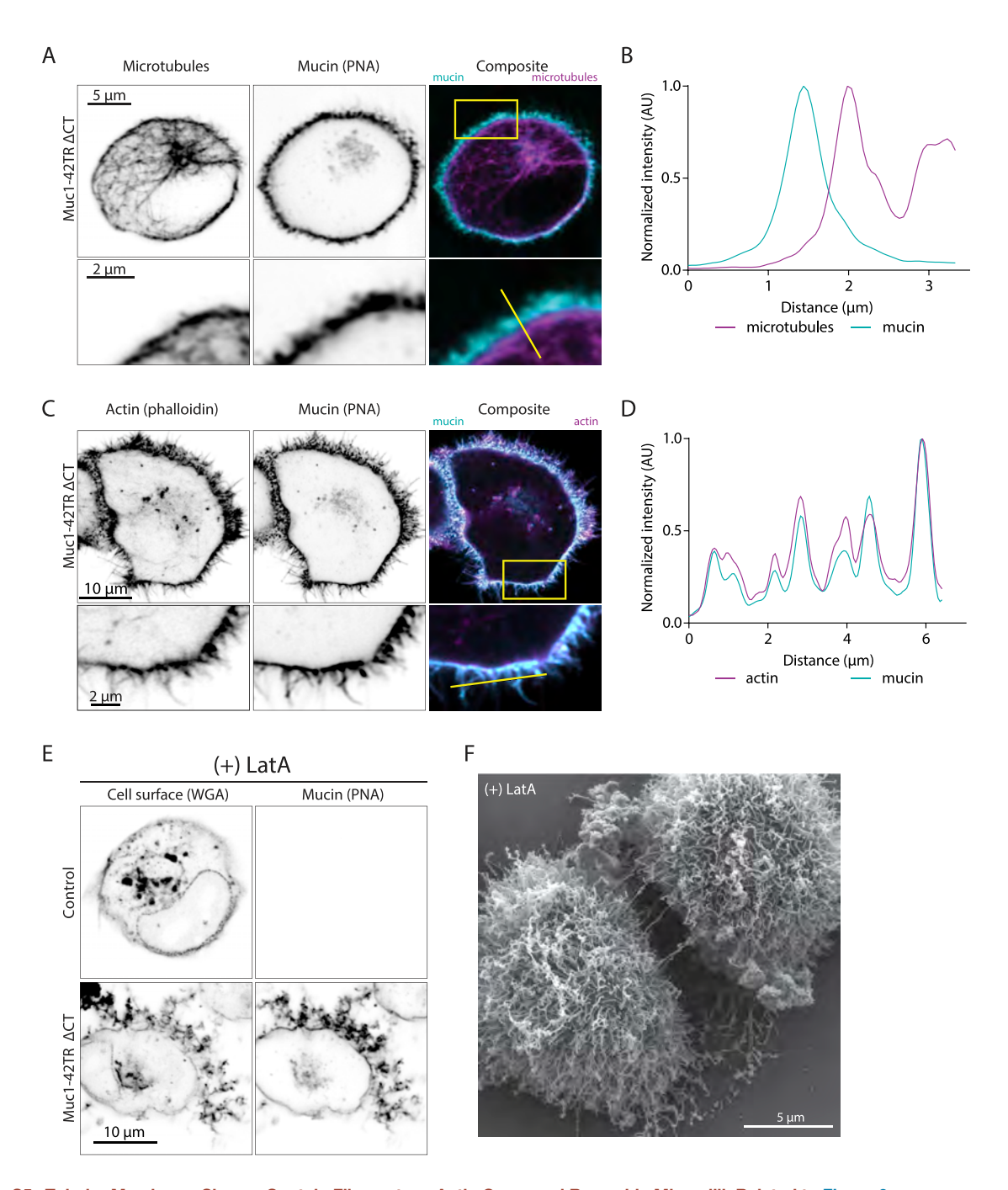


Figure S5. Tubular Membrane Shapes Contain Filamentous Actin Cores and Resemble Microvilli, Related to Figure 6

(A) Representative confocal microscopy images of epithelial cells expressing Muc1-42TR Δ CT showing indirect microtubule staining with anti-microtubule and Alexa Fluor 568-labeled secondary antibodies. Mucins are labeled with Alexa Fluor 647 PNA (peanut agglutinin). The bottom row shows the region of interest from the composite image (yellow box), n = 3.

- (B) Fluorescent intensity line trace from (A) (bottom row, yellow line). Values are normalized for their respective maximum intensities.
- (C) Representative confocal microscopy images of epithelial cells expressing Muc1-42TR Δ CT showing actin staining with Alexa Fluor 568 phalloidin. Mucins are labeled with Alexa Fluor 647 PNA. The bottom row shows the region of interest from the composite image (yellow box), n = 3. These data repeat and elaborate on (Figures 6A and 6B).
- (D) Fluorescent intensity line trace from (C) (bottom row, yellow line). Values are normalized for their respective maximum intensities.
- (E) Representative confocal microscopy images of the midplane of wild-type (Control) or Muc1-42TR Δ CT cells which have been treated with 10 μ M Latrunculin-A (LatA) for 1 h, n = 3.
- (F) Representative SEM image of LatA treated Muc1-42TR Δ CT cells.